

Hydrous carbonate-containing brucite (HCB) in MgO/hydromagnesite blends

Alexander German^{a,b,*}, Frank Winnefeld^a, Pietro Lura^{a,b}, Daniel Rentsch^c, Barbara Lothenbach^{a,d}

^a Empa, Swiss Federal Laboratories for Materials Science and Technology, Laboratory for Concrete and Asphalt, 8600 Dübendorf, Switzerland

^b ETH Zurich, Institute for Building Materials, 8093 Zurich, Switzerland

^c Empa, Swiss Federal Laboratories for Materials Science and Technology, Laboratory for Functional Polymers, 8600 Dübendorf, Switzerland

^d NTNU, Department of Structural Engineering, Trondheim, Norway

ARTICLE INFO

Keywords:

Cement
Low-carbon
Hydration
Magnesium silicates
Sequestration
Magnesium oxide
Hydromagnesite
Brucite

ABSTRACT

The hydration of reactive MgO in presence of hydromagnesite was investigated using analyses of the solid and the liquid phase. A brucite-like phase with low crystallinity was identified as hydration product. A partial destabilization of hydromagnesite was observed and it is suggested that the carbonate was taken up by the brucite-like phase. Furthermore, it was evidenced by thermogravimetry that this phase contained loosely bound “gel water”. Thus, a hypothetical *hydrous carbonate-containing brucite* (HCB) phase is proposed with a tentative composition $\text{MgCO}_3 \cdot 35\text{Mg}(\text{OH})_2 \cdot \text{H}_2\text{O}$ derived from mass balance calculations. Based on the solution chemistry and other considerations, its thermodynamic data were determined. Thermodynamic modeling of the hydrate assemblage of MgO/hydromagnesite blends confirmed the stability of HCB in the presence of hydromagnesite and brucite.

1. Introduction

The principle of mineral sequestration is based on using captured CO_2 as carbonation source for inorganic minerals [1–4]. An outstanding candidate for mineral sequestration is ultramafic rocks. These rocks contain a large fraction of the Mg-silicate mineral olivine, which is a solid solution between forsterite (Mg_2SiO_4) and fayalite (Fe_2SiO_4). Tectonic processes are able to transport ultramafic rocks to the Earth's surface leading to the formation of outcrops, which can be found in orogenic belts or as part of ophiolites (tectonically uplifted fragments of oceanic crust) [5]. Exposed to circulating hot fluids during the tectonic uplift in the crust or due to weathering at the surface, olivine-rich ultramafic rocks undergo hydrothermal alteration, which results in the conversion of olivine to serpentine ($\text{Mg}_3\text{Si}_2\text{O}_5(\text{OH})_4$) and the formation of metamorphic rocks classified as serpentinites. Both, ultramafic rocks and their metamorphic equivalent, the serpentinite offer a vast amount of Mg-silicate resources, which are distributed worldwide and which can be used for mineral sequestration [6]. However, also other Mg sources can be used to obtain precursors for mineral sequestration. Mg-rich

industrial waste products such as rejected brines from desalination plants could be valuable resources in arid regions [7–10].

Carbonation of olivine or serpentine can artificially bind CO_2 in magnesite (MgCO_3) and hydrated Mg-carbonates (HMCs) such as nesquehonite ($\text{MgCO}_3 \cdot 3\text{H}_2\text{O}$), lansfordite ($\text{MgCO}_3 \cdot 5\text{H}_2\text{O}$), artinite ($\text{Mg}_2(\text{CO}_3)(\text{OH})_2 \cdot 3\text{H}_2\text{O}$), hydromagnesite (abbreviated as HY, $\text{Mg}_5(\text{CO}_3)_4(\text{OH})_2 \cdot 4\text{H}_2\text{O}$), or dypingite ($\text{Mg}_5(\text{CO}_3)_4(\text{OH})_2 \cdot 5\text{H}_2\text{O}$). The conversion of Mg-silicates or Mg-containing solution through carbonation and subsequent calcination to MgO is a process in which no fossil-bound CO_2 (excluding potential combustion of fossil fuel for energy production) is released. The obtained Mg-carbonates can be used either as a carbon sink, i.e. the minerals are disposed as landfill after carbonation, or they can provide new raw materials for industrial applications. A possible application of Mg-carbonates in the construction industry is the production of reactive magnesia (MgO) by calcination [11]. Thus, binders based on MgO, i.e. magnesium oxide derived from magnesium silicates (MOMS) [12], offer a possibility to produce a binder raw material with a reduced carbon footprint, in contrast to Portland cement (PC) manufacture, which involves calcination of limestone. Extracted MgO can be

* Corresponding author at: Empa, Swiss Federal Laboratories for Materials Science and Technology, Laboratory for Concrete and Asphalt, 8600 Dübendorf, Switzerland.

E-mail address: german.alex@web.de (A. German).

<https://doi.org/10.1016/j.cemconres.2023.107304>

Received 2 May 2023; Received in revised form 25 July 2023; Accepted 8 August 2023

0008-8846/© 2023 The Authors. Published by Elsevier Ltd. This is an open access article under the CC BY license (<http://creativecommons.org/licenses/by/4.0/>).

utilized as raw material for Mg-based binders, the most prominent being Mg-phosphate cements (MPC), Mg-oxysulfate cements (MOS), Mg-silicate hydrate (M-S-H) cements, and the first Mg-binder patented by Sorel [13] in 1866, the Mg-oxychloride (MOC) cements [11,14].

A recently added member to the Mg-binder family are reactive MgO/basic Mg-carbonate blends,¹ which were first reported and patented by Vlasopoulos and Cheeseman in 2009 [15]. The patent describes the reactive MgO/basic Mg-carbonate blends as being a hydraulic binder, i. e. a binder that sets and hardens when mixed with water and retains its strength and stability in presence of water. The main raw material used in these blends is reactive MgO, which forms brucite ($\text{Mg}(\text{OH})_2$) during hydration. Hydration of pure MgO leads to formation of a thin brucite film on the surface of MgO, thus slowing down further dissolution and hydration. This leads to a material that lacks cohesion entirely. However, the addition of basic Mg-carbonates prevents the formation of this brucite film, leading to fast dissolution and hydration of MgO grains resulting in high cohesion in the potential building material [15]. Moreover, in presence of basic Mg-carbonates, brucite crystals grow in a low crystalline form [15–17] and show a rosette-like shaped crystal morphology [15,17,18]. It was suggested that this unique crystal morphology results in the intergrowth of many brucite crystals, thus resulting in strength development in MgO/basic Mg-carbonate blends [15,17]. Kuenzel et al. [17] tested compressive strength of MgO/HY pastes with mass mixing ratios of 9:1, 8:2, 7:3 MgO/HY and water-to-cement (w/c) ratios of 0.62. Strength values of about 18 and 24 MPa were reached after 7 and 28 d, respectively. Winnefeld et al. [16] reported compressive strength values of approximately 18 MPa after 7 d and 21 MPa after 28 d of MgO/HY mortars of 7:3 mixing ratios, w/c = 0.70, and use of superplasticisers (3 % by mass). A more recent study of Winnefeld et al. [19] reported about 40 MPa after 28 d for MgO/HY mortars without disclosing the mortar mixing recipe.

Economical production of MOMS remains the key obstacle for implementation of this binder [11,12,20,21]. Even if the CO_2 net balance remains positive with today's state of the art technologies, MOMS-based binders have the potential to be produced with a lower carbon footprint than PC in the future. There are several proposed technological processes of MgO or MgO precursors recovery, e.g. brucite, magnesite or HMCs [6,22–25]. Examples for such processes are the NETL (National Energy Technology Laboratory, US) or ÅAU (Åbo Akademi University, Finland) process [12,23]. The NETL process involves carbonation of a Mg-silicate mineral slurry at 185 °C and CO_2 pressure of 150 bars (0.317 CO_2e). The ÅAU process reaches higher efficiency (0.483 CO_2e) by using ammonium- or bisulfate, which reacts with Mg-silicates at 400 °C forming Mg-sulfates, which subsequently are precipitated as brucite by reaction with ammonia and converted to magnesite at 500–550 °C and a pressure of 20 bars. Up to date, the proposed processes do not offer a carbon-neutral technology to obtain MgO from Mg-silicates. In case economical and technological feasibility of MOMS production is accomplished, it would be desirable to put MOMS-based binders quickly into use to face the rapid developing climate crisis. Hence, MOMS-based binders have to be investigated prior to the industrial realization of CO_2 sequestration technologies with Mg-silicates. Many open research questions regard in particular hydration processes and binder performance, e.g. mechanical properties and durability.

Up to date only a few studies dealt with hydration processes of these blends [16–18,26]. A central issue is the nature of hydration products and their impact on strength development. While the patent of Vlasopoulos and Cheeseman [15] reports two stages of strengthening, e.g. intergrowth of brucite crystals and carbonation, other authors emphasize that formation of brucite is accompanied by the formation of an amorphous phase, which might provide further strength [17]. Kuenzel et al. [17] and Winnefeld et al. [16] both found that the sole hydration

products are a poorly crystalline brucite and potentially an amorphous phase with an unknown chemical composition. Furthermore, Winnefeld et al. [16] showed by thermodynamic modeling that in presence of excess water brucite, artinite, and HY occur as stable hydrates in the MgO/HY system. The presence of artinite, however, was not confirmed experimentally, most likely because its formation is kinetically hindered. To facilitate artinite formation, Winnefeld et al. [16] conducted hydration experiments with (i) artinite seeds from a geological sample and (ii) sodium bicarbonate (NaHCO_3) additions to increase the probability of HMC formation by saturating the solution with HCO_3^- ions. However, none of these approaches led to artinite formation or to the formation of any other HMC, i.e. the previously reported amorphous phase.

To clarify which hydration products are formed in hydrated MgO/HY blends, this study focuses on the analysis of hydrated MgO/HY pastes. The pastes were prepared using various mixing ratios of MgO:HY to examine the phase assemblage in respect to the HY content. To cover a wide range of mixing ratios, the following samples were prepared: 100/0, 90/10, 70/30, 50/50, 20/80 MgO/HY by mass. The 100/0 sample (pure MgO) was used as a reference, while a pure HY sample was not included, since HY does not show any cementitious properties. All samples were cured in sealed plastic vessels at 20 °C for 1, 2, 4, 6, and 12 months. To additionally study the effect of temperature on hydration, two binder compositions, 70/30 and 20/80, were selected for curing at 7, 40, and 60 °C. The low curing temperature of 7 °C was chosen to represent a cooler curing environment and curing temperatures of 40 and 60 °C (typical for dense structures) were selected to see if certain phases are preferably forming at higher temperatures. Analysis of pastes was supplemented by the analysis of suspension samples prepared for a thermodynamic study, in which the solubility of hydration products was examined. Solids obtained from suspensions (solid residues from filtration) were briefly compared with the paste samples to ensure that phase assemblages of both sample types were identical. In total, samples of five MgO/HY mixing ratios of two sample types (pastes and suspensions) cured at 20 °C and two MgO/HY mixing ratios of pastes and suspensions cured at 7, 40, and 60 °C were analyzed after 1, 2, 4, 6, and 12 months (in total: 110 samples). In this study, mainly the results for the samples hydrated for 12 months are reported, as they are closest to complete hydration and in case of the suspensions to thermodynamic equilibrium.

2. Materials and methods

2.1. Materials

Reactive MgO was prepared following the preparation procedure applied by [16]: Laboratory-grade brucite powder (Fisher Scientific, UK) was heated at 900 °C for 6 h in a static lab furnace. The high firing temperature and long residence time ensured a high purity of MgO, mitigating interference of impurities during analyses. The basic Mg-carbonate used for this study was a laboratory-grade HY from Alfa Aesar, Germany. Table 1 summarizes chemical composition, bulk density, and specific surface area (SSA) of brucite, MgO, and HY. X-ray fluorescence (XRF) measurements of MgO and HY confirmed the high purity of the used raw materials. Main oxide mass fractions determined for MgO were 98.39 wt% MgO and 0.12 wt% CaO. XRF and combustion experiments linked to infrared (IR) measurements of the HY yielded an oxide mass fraction of 42.95 wt% MgO and 35.5 wt% CO_2 , matching theoretical mass oxide fractions of HY (43.09 wt% MgO and 37.6 wt% CO_2).

Particle size distributions were measured with a laser particle size analyzer (Malvern Mastersizer X, results see Fig. S1 in the Electronic Supplementary Materials = ESM). The powders were dispersed in isopropanol by ultrasound prior to the measurement. Phase purity of raw materials was examined by X-ray diffraction (XRD) (Figs. S2–4 in the ESM). It was found that the brucite contained traces of a Mg-carbonate, most probably HY from the manufacturing process. Burning of brucite

¹ Common basic Mg-carbonates appropriate for the use in these blends are artinite, hydromagnesite or dypingite.

Table 1
Chemical composition, bulk density, SSA of raw materials.

Oxide content [mass%] ^a	Brucite	MgO	HY
SiO ₂	<0.11	<0.81	<0.11
Al ₂ O ₃	<0.11	<0.76	<0.11
Fe ₂ O ₃	<0.04	<0.11	<0.04
Cr ₂ O ₃	<0.003	<0.003	<0.003
MnO	<0.004	<0.004	<0.004
TiO ₂	<0.019	<0.04	<0.019
P ₂ O ₅	<0.017	<0.06	<0.017
CaO	0.09	0.12	0.13
MgO	68.63	98.39	42.95
K ₂ O	<0.03	<0.04	<0.03
Na ₂ O	0.24	<0.18	0.43
SO ₃	0.15	0.20	0.32
LOI	30.78	1.20	56.1
Sum	99.89	99.91	99.92
CO ₂ [mass%] ^b	1.5	2.2	35.5
bulk density [g/cm ³] ^c	2.35	3.54	1.99
SSA [m ² /g] ^d	4.29	24.3	9.51

^a Oxide contents and LOI (loss on ignition) were determined by X-ray fluorescence (XRF) according to EN 196-2.

^b Total carbon was determined according to DIN ISO 10694. Total carbon was used to calculate mass fraction [mass%] of CO₂.

^c Bulk density was determined according EN 196-6 by pycnometric method.

^d SSA was determined by nitrogen gas adsorption measurements (BET).

yielded a pure MgO powder with a SSA of 24.3 m²/g corresponding to a medium reactivity (10 m²/g ≤ SSA of medium reactive MgO ≤ 60 m²/g [14]).

2.2. Methods

2.2.1. Sample preparation

In this study the solid phase analyses of pastes and the liquid phase analyses of suspensions supplemented by solid phase analyses of the residual solids obtained by filtration of suspensions were performed. Paste and suspension samples were prepared according to MgO:HY mixing ratios of 100/0, 90/10, 70/30, 50/50, 20/80 by mass. A consequence of the high reactivity of the MgO powder was a high water demand when preparing the samples. To obtain sufficiently workable pastes, a water-to-cement (w/c) ratio of 1.20 was chosen (w/c = 20 for suspensions).

Filtration of suspensions was performed using a 0.45 µm Nylon filter (diameter: 47 mm) and pressurized air. The pH of obtained liquid phases (stock solutions) was measured directly after filtration. Stock solutions were subsequently diluted for further analysis with ion chromatography (IC) and inorganic carbon measurements.

Solid residues from filtration of the suspensions (these filter residues are named “suspensions” thereafter) and hydrated pastes were stopped by solvent exchange with isopropanol and diethyl ether adapted after a RILEM recommendation [27]. Free water was removed by immersion of crushed solid material in isopropanol for 20 min with subsequent vacuum filtration using above-mentioned Nylon filters. Isopropanol was replaced by diethyl ether via two 10 min immersion and filtration cycles. The obtained samples were then dried at 40 °C for 20 min [27]. The dried samples were ground using an agate pestle and mortar to a particle size of below 63 µm.

2.2.2. Isothermal calorimetry

A TAM Air isothermal conduction calorimeter was used to monitor heat development during hydration at 20 °C. Pastes were prepared by external mixing in glass vials. 6–8 g of homogenized MgO and MgO/HY powders were mixed with purified water (Milli-Q water) with a w/c = 1.20. The mixing was performed with a spatula by hand for 2 min. After mixing, glass vials were sealed, transferred into the calorimeter and measured for 72 h. Cumulative heat was calculated by integration of heat flow data, excluding the first 30 min after mixing due to external

mixing. Degree of hydration of MgO pastes was obtained by comparing cumulative heat values after 72 h with the theoretical hydration enthalpy of MgO to brucite (930 J/g) [28]. Degree of hydration of pastes containing HY was estimated by the same procedure applied for MgO pastes, neglecting the participation of HY in the hydration process, since HY was generally far less reactive than MgO.

2.2.3. Solid phase analyses

2.2.3.1. Thermogravimetry. 50–60 mg of powder was measured with a TGA instrument STA 449 F3 Jupiter (Netzsch, Germany) coupled with an IR Alpha detector (Bruker AG, Germany) for gas analysis. Samples were filled into alumina (Al₂O₃) crucibles (300 µl volume) and were heated from 30 to 1000 °C with a heating rate of 10 K/min in nitrogen gas atmosphere (20 ml/min). IR signals linked to H₂O and CO₂ absorbance of calibration compounds and samples from the study were determined by integrating the spectra at a wavenumber range of 1300–2000 cm^{−1} and 2200–2400 cm^{−1}, respectively.

2.2.3.2. X-ray diffraction (XRD). Crystalline phases of powder samples were examined by XRD. The measurements were conducted with a diffractometer X'Pert Pro (Malvern Panalytical, UK) in Bragg-Brentano geometry using a scanning line detector X'Celerator (Malvern Panalytical, UK). The Cu X-ray tube was operated at 45 kV and 40 mA. X-rays were monochromatized to CuK_{α1} radiation (λ = 1.54059 Å) by a Ge (111) Johansson monochromator. Samples were scanned at diffraction angles of 2θ = 5–75° with a measurement time 38.57 s per 1° resulting in a total measurement time of 45 min. Calcium fluoride (CaF₂) was used as external standard to correct the intensities due to tube decay.

2.2.3.3. Fourier-transform infrared (FTIR) spectroscopy. FTIR measurements on powders were performed using an ALPHA II FTIR-ATR instrument (Bruker AG, Germany). A diamond crystal with a reflective index of n = 2.43 was used for the measurements. 10–15 mg of powder was placed on the ATR crystal and compressed with an anvil to bring the samples into close contact with the crystal. The majority of measurements were performed at a wavenumber range of 4000–600 cm^{−1}, with the number of scans and resolution set to 32 and 4 cm^{−1}, respectively.

2.2.3.4. Raman spectroscopy. Raman spectroscopy of powders was performed using a WITec Raman spectrometer microscope (Zeiss, Germany). Specimens were placed on a microscope slide and optical focusing was done using an objective magnification of 100× (0.31 mm working distance) and performing vertical line scans along the z-axis to find the optimum height of the sample stage. The powders were irradiated with a laser of 532 nm wavelength operating at a laser power of 42 mW. Optical grating comprised 600 grooves per millimeter (g/mm) with a blaze wavelength of 500 nm. Integration time and number of scans were fixed to 16 s and 10 scans, respectively. Background correction was applied on each obtained Raman spectrum.

2.2.3.5. Solid state ¹³C nuclear magnetic resonance (NMR). ¹³C cross-polarization magic angle spinning nuclear magnetic resonance spectroscopy (¹³C CP-MAS NMR) was used to identify potentially formed HMCs and to calculate the HY amount in hydrated samples. Selected samples were measured directly after hydration stoppage and approximately 2 years after hydration stoppage (the latter is presented in this study due to a more complete dataset). However, samples measured after 2 years showed aging effects, which are described in the Results section.

NMR measurements of powders were conducted using a Bruker Advance III 400 NMR spectrometer (Bruker BioSpin AG, Switzerland). 120–340 mg of material was measured on a 7 mm CP-MAS NMR probe at 4000 Hz MAS rotation rates. For samples that could not be packed compactly enough into the 7 mm MAS rotors, smoother rotation was

achieved by the use of 3 mm thick Teflon spacers. All ^{13}C CP-MAS NMR data were recorded at 100.6 MHz, applying the following parameters: $6.0\ \mu\text{s}$ 90° excitation pulse on the ^1H channel (41 kHz), 2 ms contact time with a 32.8 kHz spin lock field on ^{13}C channel and on the proton channel ramps from 100 to 50 % of power level (spin lock field of 43 to 22 kHz), and 3 s repetition time. During acquisition 41 kHz SPINAL 64 proton decoupling was applied, and 3072–20,480 scans were recorded for a reasonable signal-to-noise ratio. The ^{13}C NMR chemical shifts were calibrated with respect to the low-frequency resonance at 29.5 ppm of an external sample with adamantane.

The absolute signal intensities of the individual spectra (integral over the entire ^{13}C NMR chemical shift region from 150 to 190 ppm of carboxylic resonances) were normalized by the weights and by the number of scans with respect to the ^{13}C CP-MAS NMR spectrum of a HY reference sample containing pure hydromagnesite starting material according to Eq. (1). The “DMFIT” software developed by Massiot et al. [29] was used to determine the relative signal intensities of NMR resonances of the individual data sets applying Lorentzian shapes. The relative amount of HY in a sample was determined by multiplying the absolute signal intensity of all carboxylic species present in a sample (see above) by the relative amount of HY in the sample obtained by line shape analysis (Eq. (2)).

$$\text{rel.amount of carboxyl species [\%]} = \frac{\text{signal intensity (sample)}}{\text{signal intensity (HY)}} \cdot \frac{\text{mass (HY)}}{\text{mass (sample)}} \cdot \frac{\text{scans (HY)}}{\text{scans (sample)}} \quad (1)$$

$$\text{HY content [\%]} = \text{rel.amount of carboxyl species} \cdot \text{rel.amount of HY signals in spectrum} \quad (2)$$

Eqs. (1) & (2) were verified by analyzing the HY content in unhydrated binders with known stoichiometry (Table S1 in the ESM).

2.2.3.6. Mass balance calculations. TGA experiments offered the possibility to retrieve additional information on phase assemblage of hydrated samples using mass balance calculations. The basis of each calculation was the fulfillment of the requirement that the total amount of the two oxides MgO and CO_2 must be equal between the unhydrated binder and the hydrated samples (Eqs. (3)–(4)).

$$m(\text{MgO})_{\text{unhyd.}} = m(\text{MgO})_{\text{hyd.}} \quad (3)$$

$$m(\text{CO}_2)_{\text{unhyd.}} = m(\text{CO}_2)_{\text{hyd.}} \quad (4)$$

This only applies if a closed system for the two oxides is considered, e.g. no matter exchange with environment involving degassing or uptake of CO_2 from the atmosphere. Mass gain due to hydration and its impact on the calculation of MgO and CO_2 weight percentage fractions in hydrated samples was taken into account by determining and applying a normalization factor (Eq. (5)). The MgO content in the hydrated binder was determined by TGA (measured residual mass).

$$\text{normalization factor} = \frac{\text{MgO content in hyd.binder}}{\text{MgO content in unhyd.binder}} \quad (5)$$

The amount of HY in a hydrated sample was obtained by dividing the mass loss measured between 500 and 550°C (major HY mass loss) of the hydrated sample by the mass loss of a HY reference in the same temperature range (Eq. (6)).

$$m(\text{HY})_{\text{hyd.}} = \frac{\text{mass loss of HY (500 – 550}^\circ\text{C)}_{\text{hyd.}}}{\text{mass loss of HY (500 – 550}^\circ\text{C)}_{\text{reference}}} \quad (6)$$

HY content obtained from TGA was used to calculate the amount of MgO, CO_2 , and H_2O bound in HY, which was subsequently subtracted from the total MgO, CO_2 , and H_2O content of the unhydrated binder. The residual MgO, CO_2 , and H_2O oxides comprised a “residue”, which represented the phase(s) formed during hydration. (Eqs. (7)–(9)).

$$m(\text{MgO})_{\text{residue}} = m(\text{MgO})_{\text{unhyd.}} - m(\text{MgO})_{\text{HY}} \quad (7)$$

$$m(\text{CO}_2)_{\text{residue}} = m(\text{CO}_2)_{\text{unhyd.}} - m(\text{CO}_2)_{\text{HY}} \quad (8)$$

$$m(\text{H}_2\text{O})_{\text{residue}} = m(\text{H}_2\text{O})_{\text{unhyd.}} - m(\text{H}_2\text{O})_{\text{HY}} \quad (9)$$

Since practically all MgO from the unhydrated binder reacted after four months, periclase was excluded from the calculation for samples of higher age, e.g. samples hydrated for 12 months. Furthermore, the amount of CO_2 bound in CaCO_3 was neglected in the calculation, since the CaO content measured by XRF in the raw materials was very low (see Table 1).

2.2.4. Liquid phase analysis

2.2.4.1. pH. pH of stock solutions was measured using a pH meter 766 (Knick, Switzerland) at ambient temperature ($22\text{--}24^\circ\text{C}$). The electrode was calibrated between a pH of 9 and 12 with two buffer solutions supplied by Merck (Germany). Since temperature has an effect on pH, all measured pH values were corrected to the designated curing temperatures of the suspensions, e.g. 7, 20, 40, 60°C . Precision of measurements was estimated from multiple measurements of stock solutions at 23.5°C to be ± 0.1 pH units.

2.2.4.2. Inorganic carbon content. Inorganic carbon content was measured with the TOC analyzer Sievers 5310C coupled to a Sievers 900 autosampler station (GE Power, Unites States (US)). Stock solution of filtered samples were diluted with purified water (Milli-Q water) to 1:10 and filled in 35 ml glass vessel for analysis. Background correction was performed by subtraction of the sample’s inorganic carbon from the value determined by measurement of pure water. As no organics were present in the samples, the total organic carbon (TOC) was negligible and therefore not reported in this study. Error of measurement ($2\text{--}5\%$) was calculated from five measurements performed for each sample by the instrument.

2.2.4.3. Ion chromatography (IC). Total concentrations of Na, K, Mg, Ca, S and Cl were measured with IC using a Dionex ICS-3000 instrument DP series (Dionex Corporation, Unites States (US)). Stock solutions of samples were diluted with purified water (Milli-Q water) to 1:10 and 1:100 directly after filtration and measured immediately to prevent alteration. The arithmetic mean between 1:10 and 1:100 dilutions was used to determine final ion concentration values. Precision of measurement was $\leq 10\%$, as reported by [30] in a previous study using the same instrument.

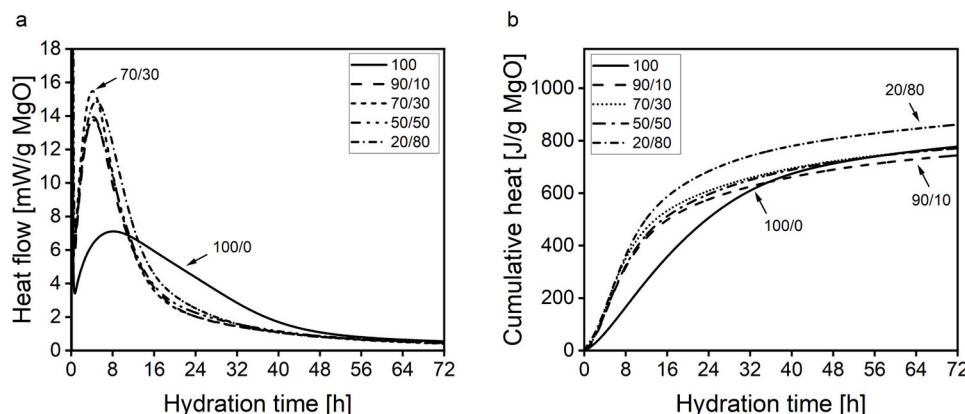
2.2.5. Thermodynamic modeling

Thermodynamic modeling was used to calculate ion activity products (IAP) and effective saturation indices (ESI) of Mg-carbonate phases based on data obtained from liquid phase analyses [31]. Calculation of IAP’s and ESI’s was performed using the Gibbs Energy Minimization Software (GEMS) for geochemical modeling [32,33]. Table 2 summarizes the thermodynamic data of Mg-phases used for computation. Modeling suppressed the formation of magnesite (MgCO_3), whose formation is kinetically hindered at ambient pressure and temperature [34], and those HMCs² [16], whose thermodynamic data remain inaccessible. Thermodynamic properties of periclase (MgO) and artinite were retrieved from the SLOP98 database [35,36]. Data for brucite and magnesite were taken from the Nagra/PSI database [37].

² Barringtonite ($\text{MgCO}_3 \cdot 2\text{H}_2\text{O}$), pokrovskite ($\text{Mg}_2(\text{CO}_3)(\text{OH})_2$), giorgiosite ($\text{Mg}_5(\text{CO}_3)_4(\text{OH})_2 \cdot 5\text{H}_2\text{O}$), unnamed dypingite-like phase ($\text{Mg}_5(\text{CO}_3)_4(\text{OH})_2 \cdot 8\text{H}_2\text{O}$), protohydromagnesite ($\text{Mg}_5(\text{CO}_3)_4(\text{OH})_2 \cdot 11\text{H}_2\text{O}$), shelkovite ($\text{Mg}_7(\text{CO}_3)_5(\text{OH})_4 \cdot 24\text{H}_2\text{O}$).

Table 2Thermodynamic data of selected inorganic phases of the MgO-CO₂-H₂O system. Values are given relative to 25 °C and 1 bar.

Phase	Chemical formulae	log K _s ^a	Δ _f G° [kJ/mol]	Δ _f H° [kJ/mol]	S° [J/(mol·K)]	C _p ° [J/(mol·K)]	V _m [cm ³ /mol]	Reference
Periclase	MgO		−569.38	−601.66	26.95	37.8	11.25	[35,36]
Brucite	Mg(OH) ₂	−11.16	−832.23	−923.27	63.14	77.28	24.63	[37]
Magnesite	MgCO ₃	−8.29	−1029.3	−1112.9	65.69	75.85	28.02	[37]
Nesquehonite	MgCO ₃ ·3H ₂ O	−5.27	−1723.6	−1981.7	180.1	237.7	74.8	[40,41]
Lansfordite	MgCO ₃ ·5H ₂ O	−5.24	−2197.8	−2574.3	249.5	317.8	103.19	[38,39]
Hydromagnesite	Mg ₅ (CO ₃) ₄ (OH) ₂ ·4H ₂ O	−37.08	−5856.8	−6514.9	478.7	526.6	208.8	[34,40]
Dypingite	Mg ₅ (CO ₃) ₄ (OH) ₂ ·5H ₂ O	−34.94	−6081.7	−6796.2	522.8	566.6	225.9	[41,42]
Artinite	Mg ₂ (CO ₃)(OH) ₂ ·3H ₂ O	−18.67	−2568.6	−2920.6	232.9	296.1	96.9	[35,36]

^a Solubility products formulated with Mg²⁺, CO₃^{2−}, OH[−] and H₂O⁰.**Fig. 1.** (a) Heat flow and (b) cumulative heat of MgO and MgO/HY pastes normalized to MgO content.

Thermodynamic properties reported for lansfordite by [38] were supplemented by density data from [39], while the heat capacity (C_p^0) value of 317.8 J/mol/K was estimated on basis of C_p^0 of nesquehonite (237.7 J/mol/K) [40] by numerical addition of the C_p^0 value of structural water ($C_p^0 = 40.04$ J/mol/K) according to [35]. Compared to our previous study [16], we have updated thermodynamic properties of nesquehonite, dypingite and HY with recent data available in open literature. Thermodynamic data of nesquehonite was used from [41] complemented by a heat capacity value reported by [40]. For dypingite [41], entropy ($S^0 = 522.8$ J/mol/K) and heat capacity ($C_p^0 = 566.6$ J/mol/K) were estimated according to [35] on basis of values from HY ($S^0 = 478.7$ J/mol/K, $C_p^0 = 526.6$ J/mol/K) and structural water ($S^0 = 40.17$ J/mol/K, $C_p^0 = 40.04$ J/mol/K). Molar volume of dypingite was determined by using the density reported by [42]. Thermodynamic properties of HY were taken from [34,40].

Correspondingly, also the volume, entropy and heat capacity of the hypothetical Mg-phase: $[\text{MgCO}_3]_{1/36}[\text{Mg}(\text{OH})_2]_{35/36}[\text{H}_2\text{O}]_{1/36}$, representing a possible composition of the hydrous carbonate-containing brucite (HCB) (see Section 4 Discussion) were estimated based on [35] from brucite and HY.

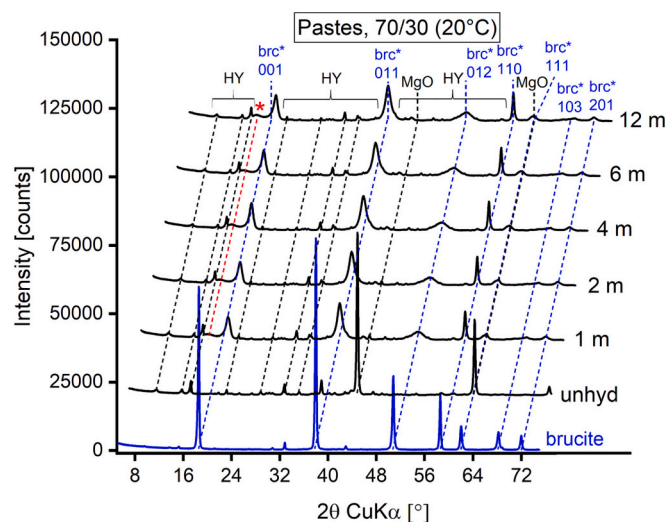
The saturation indices of brucite, nesquehonite, lansfordite, HY, dypingite, and artinite: $\text{SI} = \log_{10}(\text{IAP}/K_{\text{SO}})$ were calculated from the measured total concentrations of magnesium and inorganic dissolved carbon in the solution and the measured hydroxide concentrations. IAP is the ion activity product calculated from the measured total solution concentrations and K_{SO} is the equilibrium solubility product as detailed in Table 2. IAP's were normalized to number of Mg atoms in chemical formulae.

The activity of Mg²⁺, CO₃^{2−}, OH[−], and H₂O⁰, {i} was calculated with the help of GEMS using the measured total concentrations and considering the formation of different aqueous complexes. The activity of a

species, {i}, equals $\{i\} = \gamma_i \cdot m_i$, where γ_i is the activity coefficient and m_i the concentration of the species or complex in mol/kg H₂O. The dimensionless activity coefficients (–), γ_i , were computed with the extended Debye-Hückel equation according to Eq. (10):

$$\log \gamma_i = \frac{-A_y z_i^2 \sqrt{I}}{1 + B_y a_i \sqrt{I}} + b_y I \quad (10)$$

A common ion-size parameter a_i of 3.72 Å for NaCl solutions and common third parameter b_y (–0.64 for NaCl electrolyte at 25 °C) as integrated in GEMS were used. z_i denotes the charge of species i , I the effective molar ionic strength, and A_y and B_y are P,T-dependent coefficients. This activity correction is applicable up to approx. 1 mol/kg_w

**Fig. 2.** Diffraction patterns of brucite (blue), unhydrated 70/30 binder and hydrated 70/30 pastes (black) cured at 20 °C for 1, 2, 4, 6, and 12 months. brucite*: poorly crystalline brucite; HY: hydromagnesite; *: hump.

³ For entropy calculations, molar volumes of compounds (dypingite, nesquehonite, structural water) were taken into account.

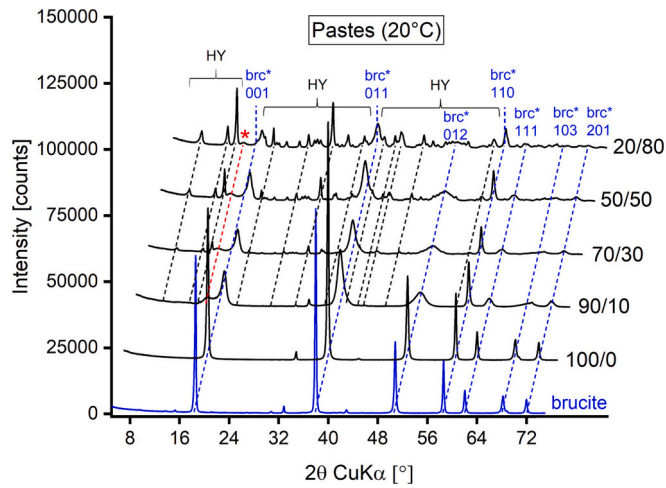


Fig. 3. Diffraction patterns of brucite (blue) and hydrated 100/0, 90/10, 70/30, 50/50, and 20/80 pastes (black) cured for 12 months at 20 °C. Red asterisk marks hump of unknown origin.

ionic strength [43].

The thermodynamic data for Mg-phases at temperatures other than 25 °C were calculated using the temperature dependence of the apparent Gibbs free energy of formation from the element, $\Delta_a G^\circ$, according to Eq. (11) [44]:

$$\Delta_a G_T^\circ = \Delta_f G_{T_0}^\circ - S_{T_0}^\circ (T - T_0) - \int_{T_0}^T \int_{T_0}^T \frac{C_p^\circ}{T} dT dT = \Delta_f G_{T_0}^\circ - S_{T_0}^\circ (T - T_0) - a_0 \left(T \ln \frac{T}{T_0} - T + T_0 \right) - 0.5 a_1 (T - T_0)^2 - a_2 \frac{(T - T_0)^2}{2T \bullet T_0^2} \quad (11)$$

where a_0 , a_1 , a_2 , and a_3 are the empirical coefficients of the heat capacity eq. $C_p^\circ = a_0 + a_1 T + a_2 T^{-2}$, T (K) the experimental temperature, while 298.15 K corresponds to the reference temperature T_0 . The apparent

Gibbs free energy of formation, $\Delta_a G^\circ_T$, corresponds at 298.15 K to the Gibbs free energy of formation, $\Delta_f G^\circ_{T_0}$. The above calculation is integrated in the GEMS-PSI code. A more detailed description of the derivation of the temperature dependence of the Gibbs energy is given in the online documentation of GEMS [32,33].

3. Results

3.1. Isothermal calorimetry

Fig. 1a shows the heat flow of MgO and MgO/HY pastes normalized to MgO content. The initial heat flow maximum could not be recorded due to external mixing. The second heat flow maximum for the MgO reference was reached after 8 h. In comparison, the second heat flow maximum of MgO/HY pastes was observed already after 6 h, showing that HY accelerated hydration at early age. Furthermore, independent of the MgO-to-HY ratio, the second heat flow maximum of measured MgO/HY pastes was recorded at the same hydration time for all samples containing HY. Heat release at the second heat flow maximum was considerably higher for MgO/HY pastes compared to the MgO reference. Differences between the four MgO/HY pastes were only marginal.

The cumulative heat curves of MgO/HY pastes show a higher increase of heat within 32 h after mixing in comparison to the MgO reference (Fig. 1b). After 32 h, 90/10, 70/30, and 50/50 MgO/HY pastes and the MgO reference exhibited similar cumulative heat values. The highest cumulative heat was measured for the 20/80 sample, its high values linked to accelerated hydration of MgO particles due to a higher water-to-MgO ratio (similar to the filler effect observed in PC pastes [45]).

Calculation of the hydration degree of the reference yielded that 84 % of MgO hydrated to brucite after 72 h. 90/10, 70/30, and 50/50 samples showed similar hydration degrees of 80, 83, and 83 %, respectively. The 20/80 sample exhibited the highest hydration degree of all samples with 93 %.

3.1.1. XRD

Impact of curing time is displayed in Fig. 2, which shows diffraction patterns of 70/30 pastes hydrated up to 12 months. Most of MgO was

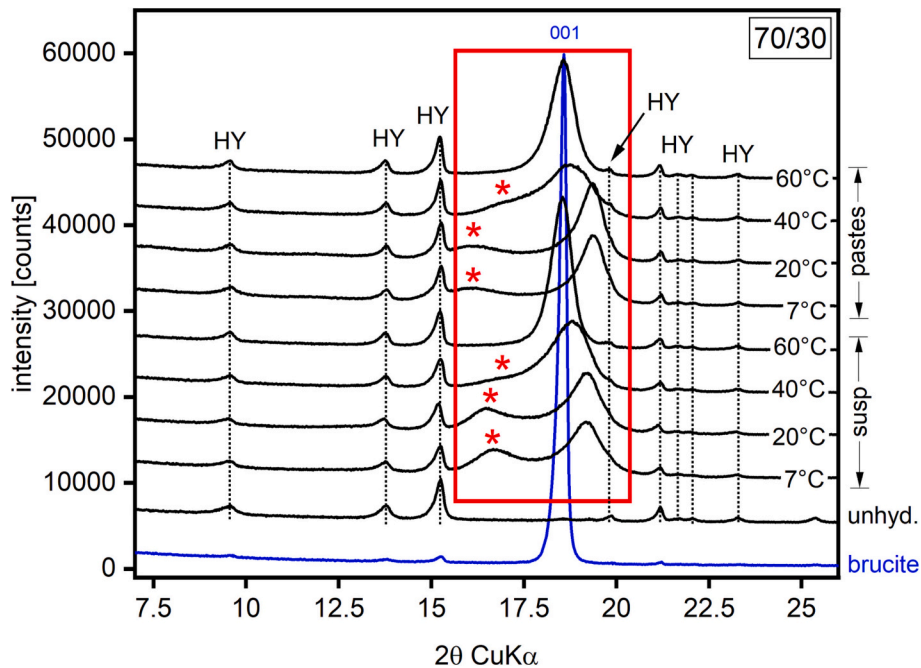


Fig. 4. Diffraction patterns of brucite (blue), unhydrated 70/30 binder, and hydrated 70/30 pastes and suspensions cured at 7, 20, 40, and 60 °C for 12 months. Red asterisk mark the position of the hump of unknown origin. Red square marks area of 001 brucite reflection and hump shifts.

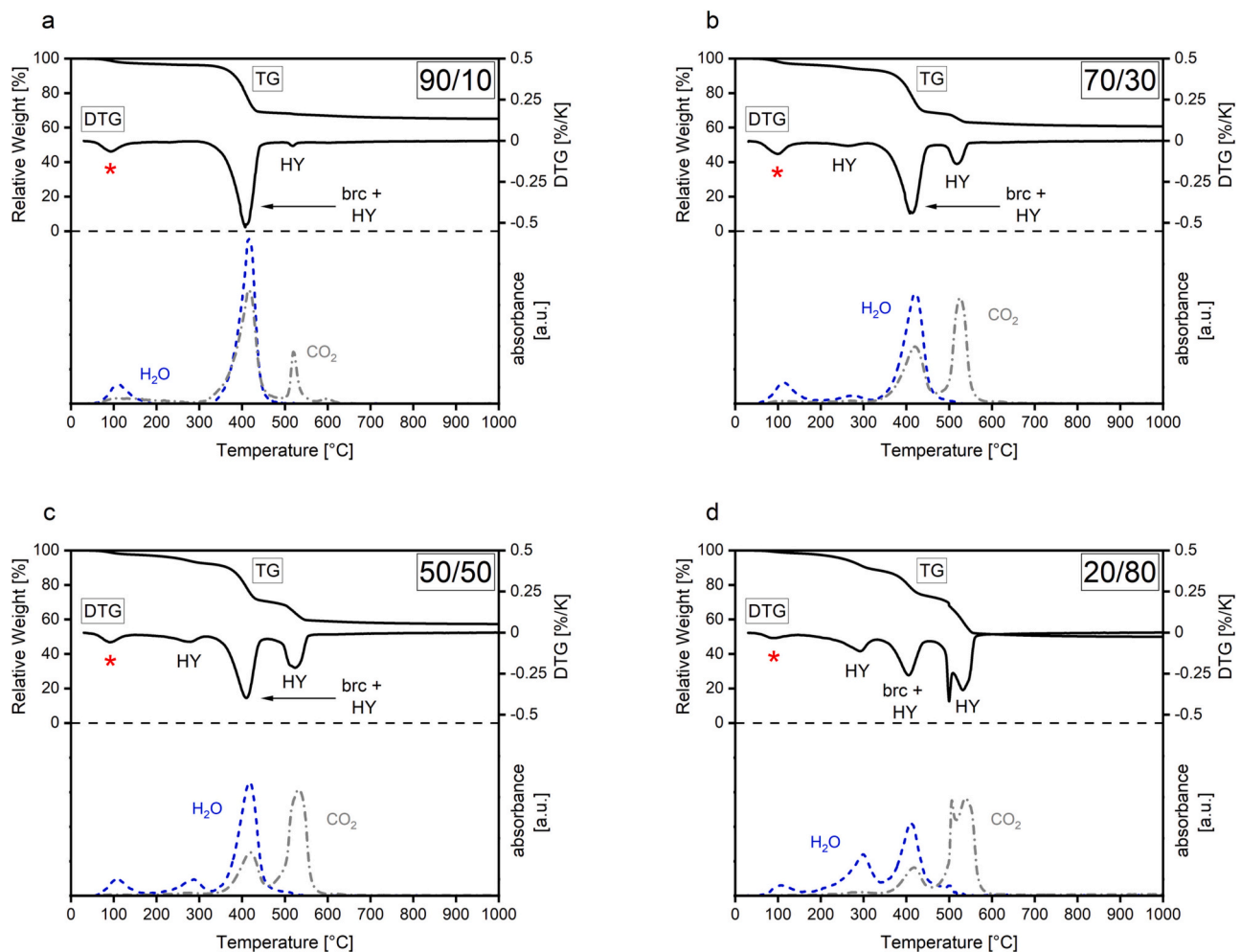


Fig. 5. TGA/FTIR data of hydrated (a) 90/10, (b) 70/30, (c) 50/50, and (d) 20/80 pastes. Samples were cured at 20 °C for 12 months. Mass loss and differential mass loss curves are displayed in the upper half of each diagram. Exhaust gas analysis of FTIR spectra recorded during TGA measurement are shown in the lower halves of the diagrams.

consumed during the first month of hydration, as was evident from a strong decrease in intensity of the 200 ($2\theta = 42.9^\circ$, $d = 2.11 \text{ \AA}$) and 220 ($2\theta = 62.2^\circ$, $d = 1.49 \text{ \AA}$) MgO reflections. Almost complete MgO consumption was reached after 4 months. On the contrary, the HY reflections change very little with time, indicating only little dissolution.

MgO reacted to brucite, whose main reflections 001, 011, 012, and 110 were observed at $2\theta = 19.3^\circ$ ($d = 4.60 \text{ \AA}$), 37.9° ($d = 2.37 \text{ \AA}$), 50.9° ($d = 1.79 \text{ \AA}$), and 58.7° ($d = 1.57 \text{ \AA}$), respectively. Brucite content did not significantly change over time, since the remaining MgO content after 28 d was rather low. The obtained brucite was less crystalline than the reference, a conclusion derived from strong broadening of several brucite reflections in the hydrated MgO/HY blends. Additionally, a shift of the 001 brucite reflection (reference: $2\theta = 18.6^\circ$, $d = 4.77 \text{ \AA}$) to higher 2θ values (19.3° , $d = 4.60 \text{ \AA}$) was observed. Such a strong shift was not observed for any other brucite reflection. Another feature was the presence of an additional, broad reflection (marked by a red asterisk) of unknown origin between $2\theta = 16.1\text{--}16.8^\circ$ ($d = 5.27\text{--}5.50 \text{ \AA}$), besides the 001 brucite reflection (see Fig. 6 in the ESM). This hump was previously addressed in literature as possible evidence for the formation of a separate, amorphous phase [16,17].

Fig. 3 shows diffraction patterns of hydrated MgO and 90/10, 70/30, 50/50, and 20/80 MgO/HY pastes cured at 20 °C for 12 months. HY was the only remaining raw material, since MgO was completely hydrated after 12 months. 90/10 blends showed practically no HY reflections, while samples with higher initial HY content clearly showed reflections

related to HY, especially the 111 and $\bar{6}01$ reflections, measured at $2\theta = 15.3^\circ$ ($d = 5.79 \text{ \AA}$) and 30.8° ($d = 2.90 \text{ \AA}$), respectively. Brucite and the hump ($2\theta = 16.1\text{--}16.4^\circ$, $d = 5.40\text{--}5.50 \text{ \AA}$) were both observed in all MgO/HY pastes, albeit present in different amounts depending on the initial MgO content, e.g. 90/10 blends having the highest brucite content and the hump being the most pronounced. Observations made from XRD analyses of pastes generally applied also to the XRD data of suspensions (Fig. S5 in the ESM). A small difference of the two sample types was found in the intensity and position of the hump. The hump showed slightly higher intensity in suspensions and was recorded at a 2θ position of $16.3\text{--}16.8^\circ$ ($d = 5.27\text{--}5.43 \text{ \AA}$), being at a higher 2θ position compared to the hump in pastes ($\Delta 2\theta = 0.2\text{--}0.4^\circ$).

XRD results of 70/30 pastes and suspensions hydrated at 7, 20, 40, and 60 °C for 12 months (Fig. 4), showed that the 2θ position of the hump depended on the curing temperature. For pastes cured at 7 and 20 °C, the maximum of the hump was positioned around $2\theta = 16.1\text{--}16.2^\circ$ ($d = 5.47\text{--}5.50 \text{ \AA}$), while the position for the maximum observed in suspensions was slightly higher: $2\theta = 16.5\text{--}16.7^\circ$ ($d = 5.30\text{--}5.37 \text{ \AA}$). The positions of the hump maxima shifted for both sample types to higher 2θ values for samples cured at 40 °C, and the hump completely vanished for samples cured at 60 °C. The curing temperature had also an effect on the 2θ position of the 001 brucite reflection. The reflection remained between $2\theta = 19.2^\circ\text{--}19.4^\circ$ ($d = 4.57\text{--}4.62 \text{ \AA}$) for pastes and samples cured at 7 and 20 °C. However, at 40 °C the position of the reflection shifted to lower 2θ values. Finally, the 001 reflection

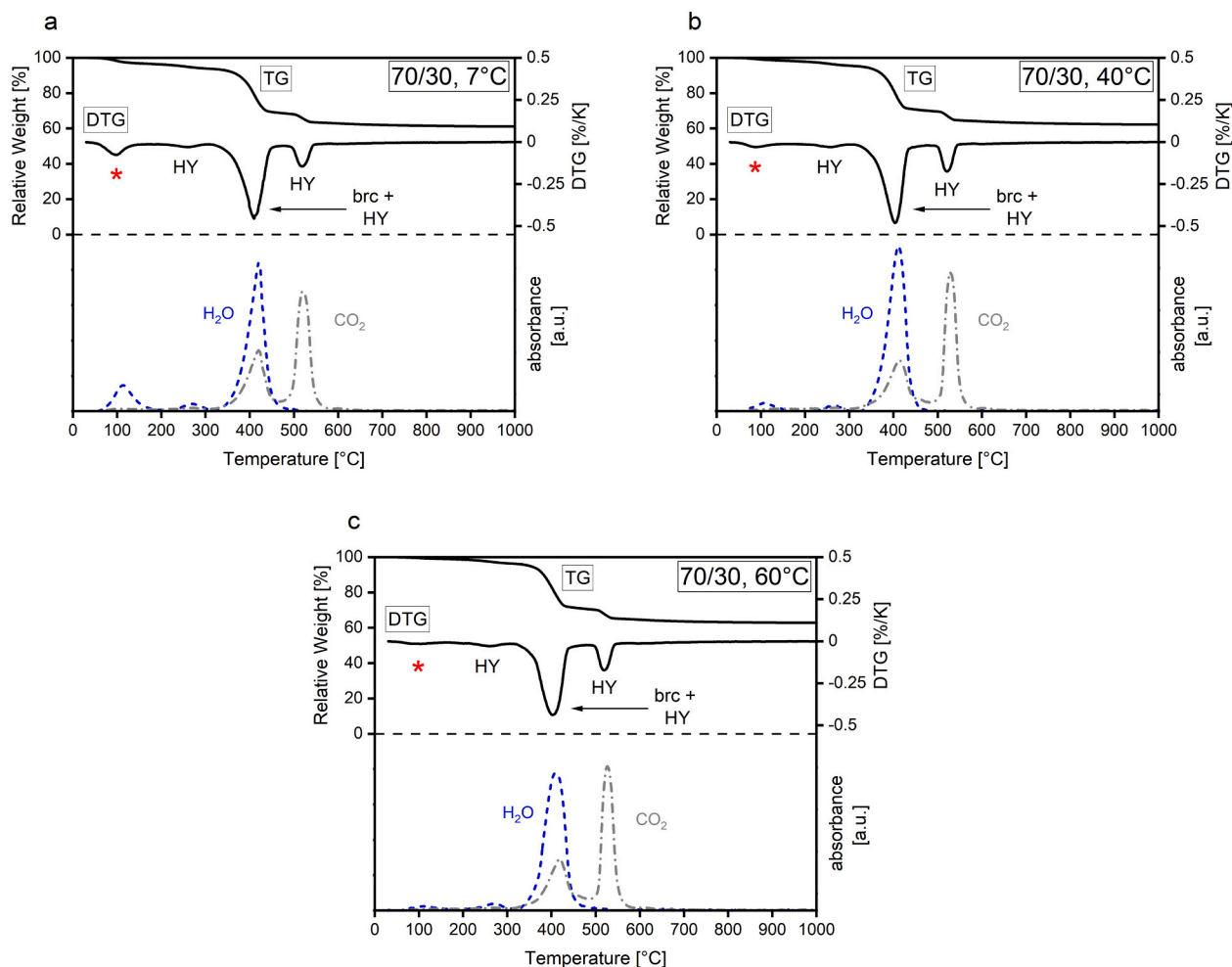


Fig. 6. TGA/FTIR data of hydrated 70/30 pastes cured at (a) 7, (b) 40, and (c) 60 °C for 12 months.

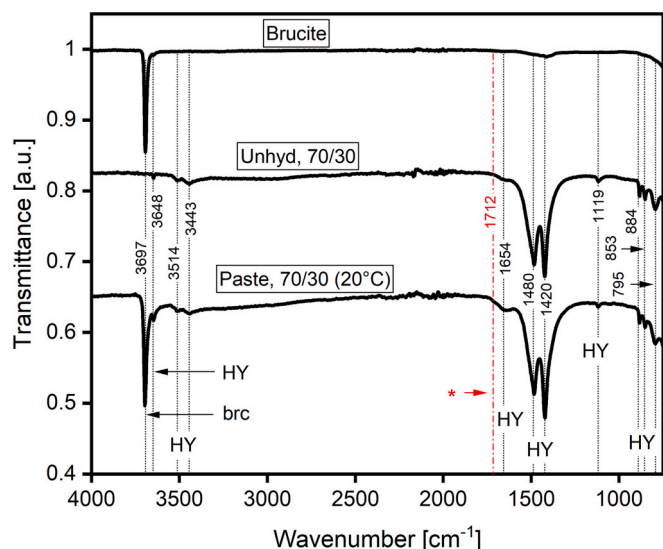


Fig. 7. FTIR spectra of a brucite reference, an unhydrated 70/30 binder, and a hydrated 70/30 paste cured at 20 °C and hydrated for 12 months.

reached the position of the brucite reference reflection at $2\theta = 18.6^\circ$ ($d = 4.77 \text{ \AA}$) for samples cured at 60 °C. Simultaneously, the intensity of the 001 reflection at 60 °C was notably higher than for all other curing temperatures.

Table 3

Observed FTIR bands in hydrated MgO/HY blends. *sh* = sharp.

Experiments		Reported in literature		
Band [cm ⁻¹]	Allocated phase	Chemical species	Vibration mode	Reference
3697 _{sh}	Brucite	OH ⁻	Asymmetric stretching	[47]
3648	HY	OH ⁻	Stretching vibrations	[48,49]
3514	HY	OH ⁻	Stretching vibrations	[48,50]
3443	HY	OH ⁻	Stretching vibrations	[48,49]
1712	Unknown	n/a	n/a	
1654	HY	H ₂ O	Bending vibration	[48,49]
1480 _{sh}	HY	CO ₃ ²⁻	ν_3 asymmetric stretching	[48–50]
1420 _{sh}	HY	CO ₃ ²⁻	ν_3 asymmetric stretching	[48–50]
1393	HY	CO ₃ ²⁻	n/a (asymmetric stretching?)	[48]
1335	(HY)	CO ₃ ²⁻	n/a	
1119	HY	CO ₃ ²⁻	ν_1 symmetric stretching	[49]
1028	Impurity	n/a	n/a	
884	HY	CO ₃ ²⁻	Bending vibration	[49,51]
853	HY	CO ₃ ²⁻	Bending vibration	[49,51]
795	HY	CO ₃ ²⁻	Bending vibration	[49,51]

3.1.2. TGA

TGA/FTIR results of hydrated 90/10, 70/30, 50/50, and 20/80 pastes cured at 20 °C for 12 months are shown in Fig. 5a–d (a hydrated 100/0 paste is displayed in Fig. S7 in the ESM). Corresponding

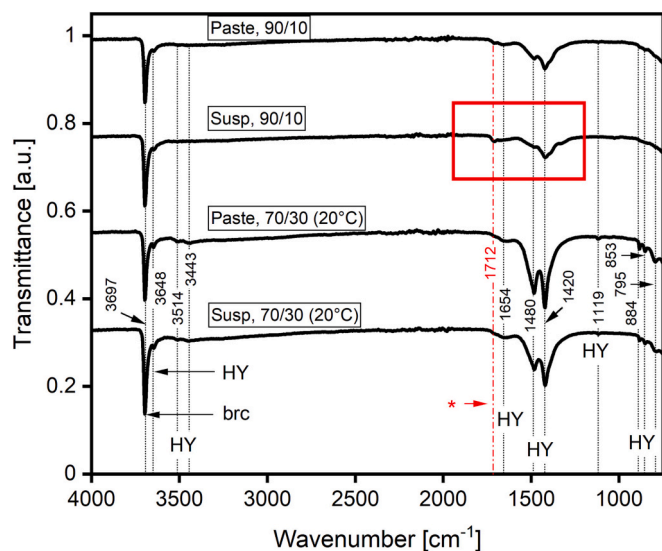


Fig. 8. FTIR spectra of 90/10 and 70/30 pastes and suspensions cured at 20 °C for 12 months. Spectral area of 90/10 suspension sample marked in a red rectangle is shown enlarged in Fig. 9.

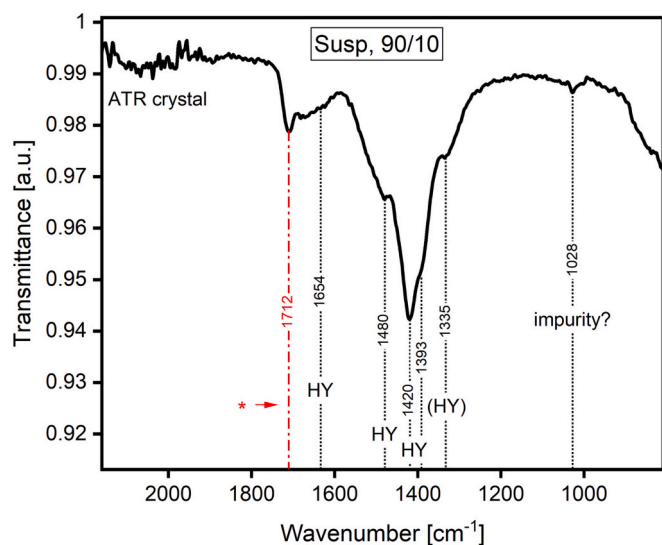


Fig. 9. Enlarged region of the FTIR spectrum of a 90/10 suspension cured at 20 °C for 12 months in the range of 810–2160 cm^{-1} .

suspension samples are presented in Fig. S8a–d in the ESM. The 90/10 paste (Fig. 5a) showed a strong decomposition peak between 300 and 480 °C. The mass loss in this temperature region can be allocated to thermal decomposition of brucite (maximum at approximately 400 °C), which was accompanied by a strong loss of water during the dehydroxylation process (as identified by FTIR in the exhaust gases). The mass loss between 500 and 550 °C was attributed to the major decarbonation step of HY.⁴ Another mass loss of unknown origin was measured between 30 and 160 °C (marked by a red asterisk). FTIR confirmed the presence of mainly H_2O in the exhaust gases in this

⁴ HY has a complex thermal decomposition behavior involving three major decomposition events: 145–355 °C (loss of crystal water), 355–455 °C (loss of crystal water and first, partial decarbonation), and 500–550 °C (dehydroxylation and second (major) decarbonation step). However, due to the low amounts of HY in the mixtures, only the major decomposition step can be detected.

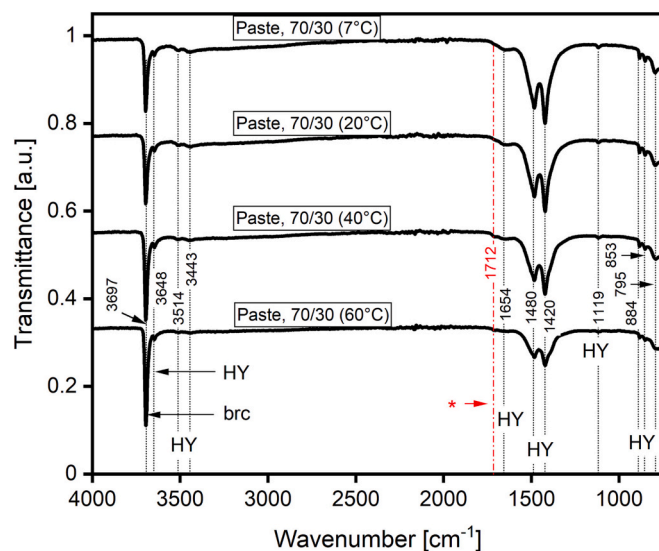


Fig. 10. FTIR spectra of 70/30 pastes cured at 7, 20, 40, and 60 °C for 12 months.

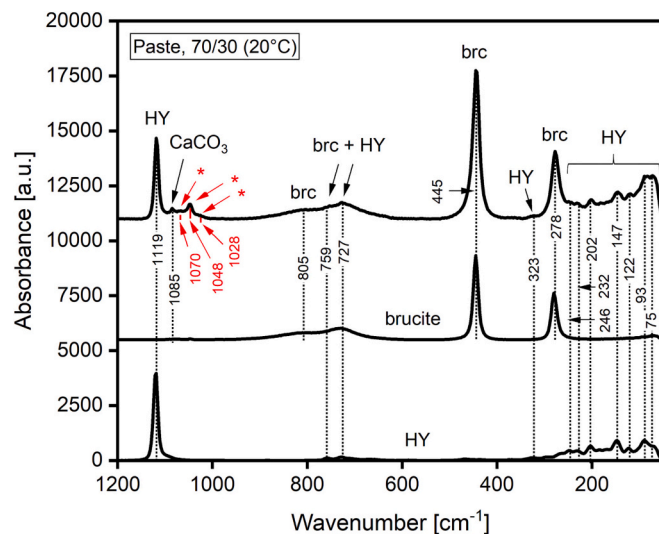


Fig. 11. Raman spectra of a 70/30 paste cured at 20 °C for 12 months (above) and two reference spectra of brucite (middle) and HY (below). Intensities of brucite and HY spectra were rescaled to prevent overlap of adjacent spectra in the diagram. Absorbance values of brucite and HY were divided by the factor 2 and 3, respectively.

temperature range. Winnefeld et al. [16] and Kuenzel et al. [17] both reported a similar mass loss in that temperature range, allocating it tentatively to the loss of loosely-bound water from a potentially formed poorly crystalline Mg-phase. Another important observation was the detection of a CO_2 IR signal between 300 and 480 °C, the temperature range where brucite dehydroxylated and where only a minor decarbonation step of HY was expected. Since the CO_2 IR signal intensity of the major HY decarbonation step between 500 and 550 °C was notably smaller than the CO_2 IR signal between 300 and 480 °C, HY decarbonation could not have had been solely responsible for the CO_2 IR signal between 300 and 480 °C. Hence, the CO_2 must have had been originated in addition from another phase (to be discussed later).

TGA/FTIR measurements of 70/30, 50/50, and 20/80 pastes cured at 20 °C yielded similar results as already reported for the 90/10 sample. The main decomposition peaks recorded for all samples were assigned to brucite and HY, the latter being dominant especially in the 20/80 sample. Decomposition of brucite and partially of HY between 300 and

Table 4Observed Raman bands in hydrated MgO/HY pastes and suspensions. *sh* = sharp.

Experiments		Reported in literature		
Band [cm^{-1}]	Allocated phase	Chemical species	Vibration mode	Reference
1119 _{sh}	HY	CO_3^{2-}	ν_1 symmetric stretching	[48]
1085	CaCO_3	CO_3^{2-}	ν_1 symmetric stretching	[54]
1070	Unknown	n/a	n/a	
1048	Unknown	n/a	n/a	
1028	Unknown	n/a	n/a	
805	brucite	OH^-	Lattice vibrations	[52,53]
790–620	HY	HCO_3^-	ν_4 bending vibrations	[48,54]
	Brucite	OH^-	Lattice vibrations	[52,53]
445 _{sh}	Brucite	OH^-	Lattice vibrations	[52,53]
323	HY	CO_3^{2-}	ν_1 symmetric stretching	[54]
278 _{sh}	Brucite	OH^-	Lattice vibrations	[52,53]
232	HY	CO_3^{2-}	ν_1 symmetric stretching	[54]
202	HY	CO_3^{2-}	ν_1 symmetric stretching	[54]
147	HY	CO_3^{2-}	ν_1 symmetric stretching	[54]
122, 93, 75	HY	CO_3^{2-}	n/a	

480 °C yielded smaller mass losses for the 70/30 (Fig. 5b) and 50/50 paste (Fig. 5c) in comparison to the 90/10 sample. The 20/80 paste (Fig. 5d) showed the lowest mass loss of all samples between 300 and 480 °C.

Partial loss of HY crystal water between 200 and 235 °C resulted in a minor decomposition peak visible in 70/30, 50/50, and 20/80 samples. The decomposition peak of HY related to further loss of crystal water and partial decarbonation between 355 and 455 °C was not visible due to an overlap with the brucite peak, while the main decomposition peak of HY was measured between 500 and 550 °C. For the 20/80 paste, the mass loss of the major HY decomposition peak exceeded the mass loss of brucite. In addition, a peak splitting was observed for the HY decomposition peak at 497 °C due to a more pronounced exothermic event of HY [46].

The decomposition peak measured between 30 and 160 °C was present in the pastes of various binder compositions. Mass loss was higher for samples with initially high MgO content, e.g. 90/10 and 70/30 samples. The 20/80 sample exhibited the lowest mass loss.

TGA/FTIR data of the 70/30 pastes hydrated at 7, 40, and 60 °C for 12 months are displayed in Fig. 6a–c, respectively. Curing at 7 °C (Fig. 6a) was similar to curing at 20 °C (Fig. 5b). Curing at 40 °C (Fig. 6b) led to a decrease of the decomposition peak measured between 30 and 160 °C. Practically no mass loss was measured at the same temperature range for samples cured at 60 °C (Fig. 6c). Thus, the phase responsible for this mass loss was nearly absent in the sample cured at 60 °C. TGA/FTIR results obtained from suspensions (Fig. S9a–c in the ESM) cured at different temperatures did not give any further insights and are therefore not discussed in detail.

Observations outlined for pastes in this section applied also for the suspensions. An exception was the occurrence of an additional mass loss at 445 °C for 90/10, 70/30, and 50/50 suspensions. Its origin remained unclear, perhaps being one of several HY decomposition steps, which was resolved in suspensions better than in paste samples.

3.1.3. Fourier-transform infrared (FTIR) spectroscopy

Fig. 7 shows an FTIR spectrum of a hydrated 70/30 paste cured at 20 °C for 12 months. Major bands were allocated to brucite and unreacted HY. Table 3 summarizes observed bands and their vibration mode of chemical species, if known. The sharp band at 3697 cm^{-1} corresponded to the O–H asymmetric stretching of the hydroxide ions of brucite [47]. Further bands from O–H stretching vibrations of hydroxide ions at 3443, 3514, and 3648 cm^{-1} were allocated to hydroxide ions present in HY [48–50]. The band at 1654 cm^{-1} was a result of bending vibrations of strongly hydrogen-bonded water molecules from HY [48]. IR Bands at 1420 and 1480 cm^{-1} were products of asymmetric stretching of CO_3^{2-} ions from HY [48–50], as most probably were bands at 1335 and 1393 cm^{-1} as well (only listed in the table). The band at

1119 cm^{-1} occurred due to symmetric stretching of CO_3^{2-} ions of HY [49]. Bands at 795, 853, and 884 cm^{-1} were assigned to CO_3^{2-} ions bending vibrations [49,51]. The noisy baseline at 1900–2300 cm^{-1} was a measurement artifact attributed to the diamond ATR crystal of the measuring device.

Signal intensities of brucite (3697 cm^{-1}) and of major HY bands (1420, 1480 cm^{-1}) were found to differ between pastes and suspensions (Fig. 8). Spectra of 90/10 and 70/30 suspensions showed lower HY signal intensities in contrast to their paste counterparts, indicating a more pronounced dissolution of HY in suspensions. While the HY signal intensities were lower, the brucite signal intensity was higher for suspensions. Hence, a higher dissolution of HY could have led to more available Mg^{2+} in solution, promoting brucite formation.

Fig. 9 shows the FTIR spectrum of the 90/10 suspension sample from Fig. 8 enlarged between 860 and 2160 cm^{-1} . A weak band of unknown origin (marked by a red asterisk) was observed at 1712 cm^{-1} . This band could not be assigned to any known HMC. Therefore, we suggest that this band must be related to the presence of an unknown phase. Judging from the wavenumber of this band, it is reasonable to assume that the band at 1712 cm^{-1} was a result of an asymmetric stretching of CO_3^{2-} ions. Thus, the unknown phase probably contained carbonate. The best resolved band of the unknown carbonate was found in 90/10 samples. In 70/30 samples, the band at 1712 cm^{-1} was only present as a shoulder, perhaps partly covered by the adjacent 1654 cm^{-1} band of HY and therefore not well visible. The band at 1028 cm^{-1} in Fig. 9 displays the presence of an impurity since it was present also in the reference sample (100 wt% MgO) and holds therefore no significance for the interpretation of the hydrated data set.

IR Spectra of 70/30 pastes cured at 7, 20, 40, and 60 °C are plotted in Fig. 10. Signal intensities of phases were similar for pastes cured at 7 and 20 °C. However, pastes cured at 40 and 60 °C showed clearly a decrease of signal intensities of HY (1420 and 1480 cm^{-1}) and a substantial increase of signal intensity of brucite at 3697 cm^{-1} . This effect can be explained by dissolution of HY at elevated temperatures followed by an enhanced formation of brucite similar to the effect observed for suspensions. Different curing temperatures did not influence signal intensity of the band at 1712 cm^{-1} assigned to the unknown carbonate. Furthermore, it was attempted to interpret the changing signal ratio between the HY signal at 1420 and 1480 cm^{-1} between samples cured at ambient and elevated temperatures. However, inspection of unhydrated samples containing low amounts of HY showed similar effects, i.e. deviations from the theoretical signal ratio between the major HY bands of a pure HY reference sample. This effect was based on the intrinsic IR behavior of the chemical compound rather than on a presence of a so far obscured band from the unknown carbonate. Finally, it was not possible to find a definitive answer if additional bands of the phase were obscured by the HY, which dominated the spectra. However, the amount

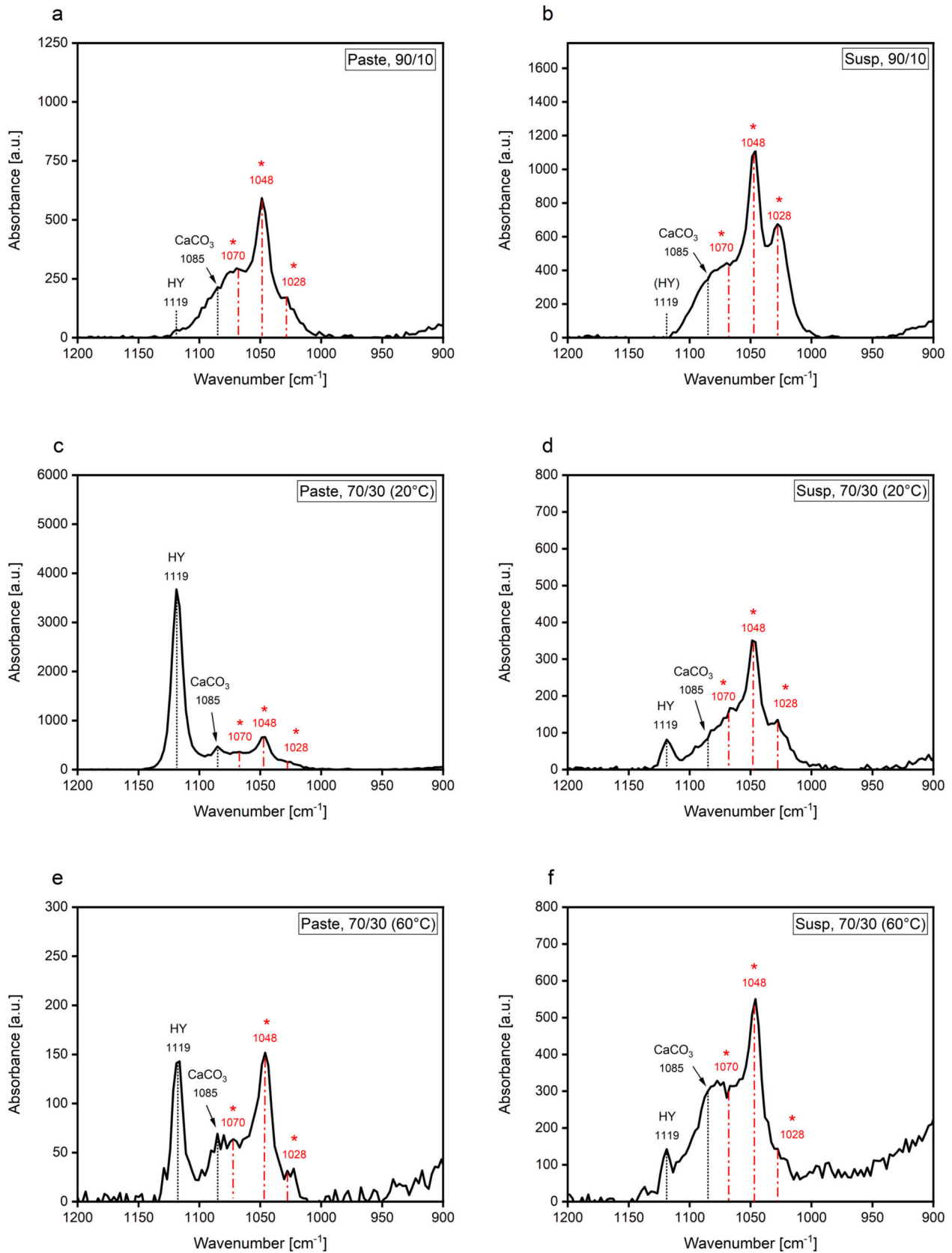


Fig. 12. Raman spectra of (a) 90/10 paste and (b) 90/10 suspension cured at 20 °C, (c) 70/30 pastes and (d) 70/30 suspensions cured at 20 °C, and (e) 70/30 pastes and (f) 70/30 suspensions cured at 60 °C. Spectra show a selected wavenumber range between 900 and 1200 cm⁻¹, which is typical for HMCs. Note the different scales of the ordinate of the spectra.

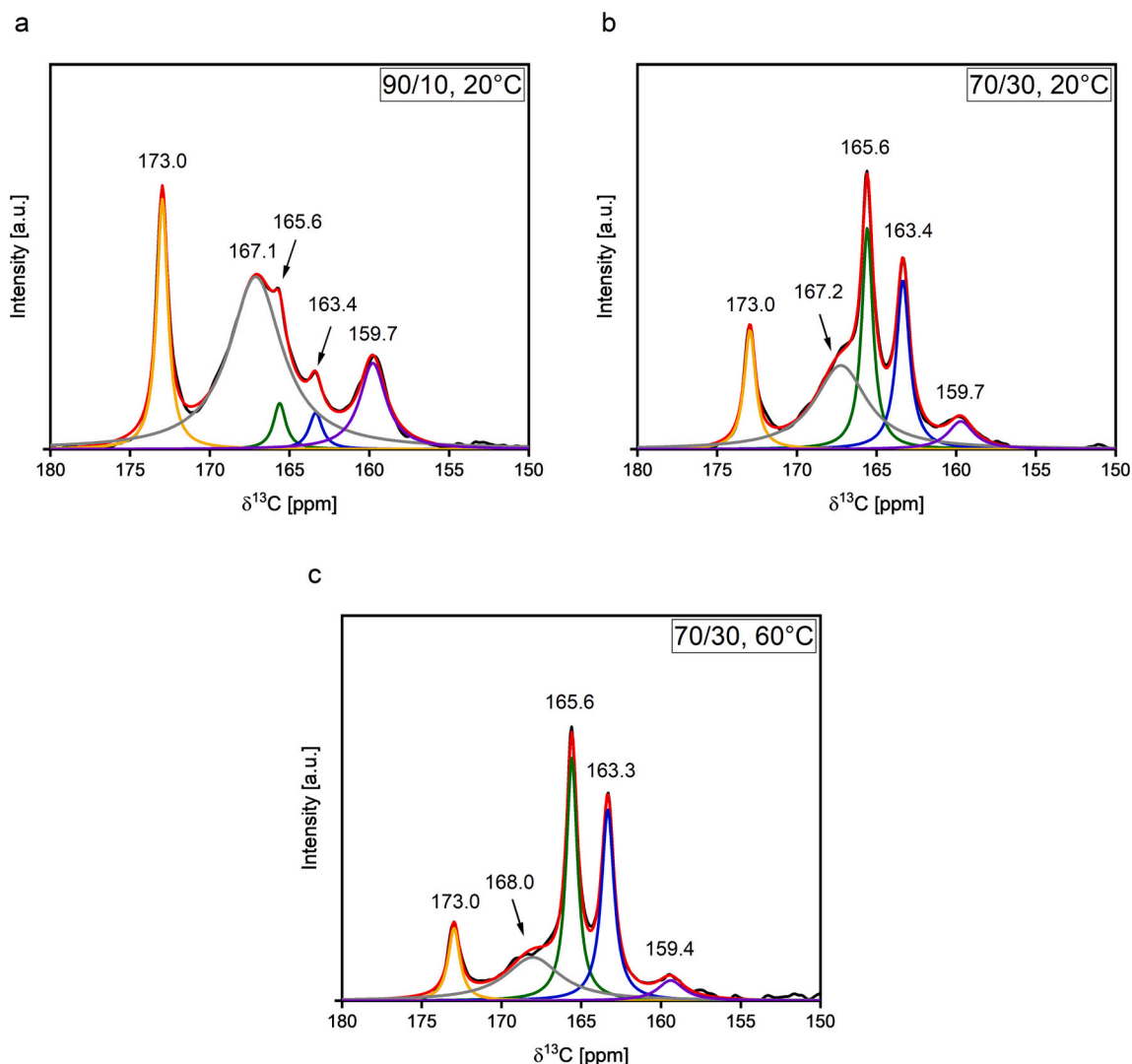


Fig. 13. ^{13}C CP-MAS NMR spectra with simulated shapes of individual resonances of (a) 90/10 paste cured at 20 °C for 12 months and 70/30 pastes cured at (b) 20 °C and (c) 60 °C for 12 months.

of the carbonate in the unknown phase must have been much lower than the amount of HY.

3.1.4. Raman spectroscopy

Fig. 11 shows a Raman spectrum of a 70/30 paste cured at 20 °C for 12 months. Observed Raman bands and corresponding vibration modes of chemical species (as far as they are known) are listed in Table 4. Two prominent Raman bands at 278 and 445 cm^{-1} were associated with brucite [52,53]. Further brucite bands were recorded at 805 cm^{-1} [52,53] and in the spectral range between 620 and 790 cm^{-1} (theoretical positions: 680 and 725 cm^{-1} [52]), where they overlapped with several HY bands from HCO_3^- ν_4 bending vibrations (644, 655, 673, 699, and 708 cm^{-1}) [54]. The unusual broadness of brucite Raman bands in the spectral range between 620 and 790 cm^{-1} is reported in literature to be due to anharmonic coupling of the 680 and 725 cm^{-1} bands to other vibration modes [52]. In general, the vibration mode responsible for brucite bands in the Raman spectrum between 50 and 1200 cm^{-1} is lattice vibration [52,53].

The main HY band, a result of CO_3^{2-} ν_1 symmetric stretching [48], was measured at 1119 cm^{-1} . HY bands of the same vibration mode were found at 147, 202, 232, and 323 cm^{-1} . At wavenumbers between 50 and 145 cm^{-1} , several overlapping HY bands were found in the paste's spectrum. The spectrum of the HY reference was used to identify the

Table 5

Observed ^{13}C CP-MAS NMR signals in hydrated MgO/HY pastes and suspensions.

Chemical shift [ppm]	Resonance/allocated phase (if known)	Reference
159.4–159.7	Carboxylic resonance A	
163.4	HY	[55,56]
165.6	HY	[55,56]
167.0–168.0	Sorbed $\text{CO}_3^{2-}/\text{HCO}_3^-$	[57,58]
173.0	Carboxylic resonance B	

bands in that spectral range: 75, 93, and 122 cm^{-1} , however, the corresponding vibration mode(s) were not found in the literature.

Another weak Raman band was detected at 1085 cm^{-1} associated with the CO_3^{2-} ν_1 symmetric stretching mode observed for CaCO_3 [54]. Although raw materials used in this study were of high purity (laboratory-grade materials), XRF (Table 1) showed traces of 0.12 and 0.13 wt % CaO in MgO and HY, respectively, thus, explaining the occurrence of the CaCO_3 band at 1085 cm^{-1} in hydrated MgO/HY samples.

Further Raman bands of unknown affiliation (marked by red asterisk) were detected in the hydrated MgO/HY samples between 1025 and 1080 cm^{-1} forming a broad Raman signal. These bands were located in a spectral range typical for HMCs [54], indicating the presence of an unknown carbonate.

Table 6

^{13}C NMR chemical shifts and relative amounts of carbonate species determined by line shape analysis of a hydrated 90/10 paste cured at 20 °C and of 70/30 pastes cured at 20 °C and 60 °C for 12 months.

	$\delta^{13}\text{C}$ [ppm]	Rel. amount [mol/mol%]	Rel. signal intensity HY [%]
<i>Paste, 90/10 (20 °C)</i>			
Carboxylic resonance A	159.7	24.7	
1st HY signal	163.4	3.1	46.2
2nd HY signal	165.6	3.6	53.8
Sorbed $\text{CO}_3^{2-}/\text{HCO}_3^-$	167.1	54.0	
Carboxylic resonance B	173.0	14.6	
<i>Paste, 70/30 (20 °C)</i>			
Carboxylic resonance A	159.7	6.5	
1st HY signal	163.4	19.9	47.3
2nd HY signal	165.6	22.2	52.7
Sorbed $\text{CO}_3^{2-}/\text{HCO}_3^-$	167.2	39.2	
Carboxylic resonance B	173.0	12.2	
<i>Paste, 70/30 (60 °C)</i>			
Carboxylic resonance A	159.4	5.9	
1st HY signal	163.3	27.1	47.0
2nd HY signal	165.6	30.6	53.0
Sorbed $\text{CO}_3^{2-}/\text{HCO}_3^-$	168.0	26.9	
Carboxylic resonance B	173.0	9.5	

Fig. 12a–f shows Raman spectra of 90/10 pastes and suspensions cured at 20 °C and 70/30 pastes and suspensions cured at 20 °C and 60 °C for 12 months. To provide better visibility of the bands affiliated to the unknown carbonate ($1025\text{--}1080\text{ cm}^{-1}$) and the major HY band at 1119 cm^{-1} , a spectral range between 900 and 1200 cm^{-1} was selected. Note that the ordinates of the spectra were scaled accordingly to the best possible visibility of peaks. Since measured intensities in the Raman spectra heavily depended on optical focusing and targeted sample grains during the measurements, it is emphasized that a comparison of intensities between Raman signals of different samples does not provide any quantitative information.

Raman spectra of a 90/10 paste and suspension are displayed in Fig. 12a & b. The HY Raman band was practically absent in both spectra, confirming that most of HY reacted during hydration. Fig. 12c–f shows spectra of 70/30 pastes and suspensions cured at 20 and 60 °C. Suspension spectra showed weak HY peaks, reflecting the low HY content in those samples in accordance to FTIR findings. Bands of the unknown carbonate located at $1025\text{--}1080\text{ cm}^{-1}$ were present in all spectra shown in Fig. 12a–f. It is suggested that the broad Raman signal at $1025\text{--}1080\text{ cm}^{-1}$ was a product of at least three bands located at 1028, 1048, and 1070 cm^{-1} (marked by red asterisks in Figs. 11 and 12a–f). In accordance to [16], the band at 1048 cm^{-1} showed the highest intensity of the triplet, while the other two bands were mainly present as shoulders of the main band at lower and higher wavenumbers. Fig. 12b provided an excellent spectrum for pinpointing the location of the band at lower wavenumbers (1028 cm^{-1}), while the position of the band at higher wavenumbers was estimated to be 1070 cm^{-1} . The reason for clearer peak visibility of the unknown carbonate in the spectra of this study compared to [16] can likely be attributed to the longer hydration time of 12 months.

3.1.5. Solid state ^{13}C CP-MAS NMR

Fig. 13a–c shows ^{13}C CP-MAS NMR spectra of a hydrated 90/10 paste cured at 20 °C and of 70/30 pastes cured at 20 °C and 60 °C for 12 months. In total, five different signals of the ^{13}C NMR chemical shift region of carboxylic groups were observed for these hydrated samples (Table 5). The two sharp resonances at 163.4 ppm and 165.6 ppm were assigned to unreacted HY [55,56] and correspond exactly to the chemical shifts of the signals determined for the HY reference (Fig. S10 in the ESM). Three further signals consisted of a broad resonance with its maximum at $167\text{--}168\text{ ppm}$ and two more narrow resonances observed

between 159.4 and 159.7 ppm (carboxylic resonance A) and at 173.0 ppm (carboxylic resonance B). The peak maximum of the broad resonance at $167\text{--}168\text{ ppm}$ was very close to the main HY peak (165.6 ppm). In literature, the origin of this signal is described as being associated to sorbed $\text{CO}_3^{2-}/\text{HCO}_3^-$ on the solid [57,58]. The signal of the carboxylic resonance A was identified as being related to aging of the samples. It was found that this resonance was not present in measurements conducted directly after hydration stoppage, however, occurred after approximately 2 years of storage in a desiccator for the same samples. Evidence is provided in Fig. S11 in the ESM, where two recorded spectra of the same sample at different periods is shown. Resonance B was tentatively assigned to a carbonate of unknown origin, since no HMC with the corresponding characteristic ^{13}C NMR chemical shift was identified in literature.

Line shape analysis of the 90/10 paste (Table 6) yielded that sorbed $\text{CO}_3^{2-}/\text{HCO}_3^-$ was the dominant carbonate species in the sample. The lowest relative amount was obtained for HY for which the resonances at 165.6 ppm and 163.4 ppm were measured.⁵

The dominant carbonate species in 70/30 pastes cured at 20 °C (Fig. 13b) and at 60 °C (Fig. 13c) was HY. The relative amount of both HY signals in the 70/30 pastes was slightly higher than the relative amount calculated for the sorbed $\text{CO}_3^{2-}/\text{HCO}_3^-$. Relative amounts of the carboxylic species related to the resonances A and B reached even lower amounts.

Spectra of suspension samples (Fig. S12 in the ESM) showed the same resonances as observed in pastes. Line shape analysis of the suspension spectra (Table S3 in the ESM) showed similar trends as for the pastes and are therefore not discussed in detail.

Data from line shape analysis of both pastes and suspensions was used to calculate the HY content in the hydrated samples using Eqs. (1) & (2) (results are summarized in Table 7). The calculation of HY content in 90/10 paste and the suspension samples yielded values of 1.6 % and 1.8 % HY for the suspensions and the paste, respectively. This result was in accordance to XRD and TGA results, in which only low amounts of HY were found. Due to their composition, 70/30 paste and the suspension samples showed as expected much higher HY contents, since a great

⁵ Note that relative signal intensities between the first and the second HY peak remained almost the same for all samples, as well as for the HY reference (see Table S2 in the ESM for line shape analysis of the HY reference).

Table 7
HY content of hydrated 90/10, 70/30, 50/50, 20/80 pastes and suspensions cured for 12 months at different temperatures.

Sample	Number of scans	Sample mass [mg]	Absolute signal intensity	Rel. amount of carboxylic species [%] ^a	Rel. amount of HY signals in spectra [%] ^b	HY content in samples [mass%] ^c
Pastes	90/10 (20 °C)	216.3	159.0	25.6	6.9	1.8
	70/30 (20 °C)	215.3	60.4	38.4	42.1	16.2
	70/30 (60 °C)	194.4	40.2	28.5	57.7	16.5
Suspensions	90/10 (20 °C)	88.4	67.5	26.6	5.9	1.6
	70/30 (20 °C)	99.2	110.4	38.7	41.9	16.2
	70/30 (60 °C)	141.5	107.8	26.5	55.3	14.7

^a Relative to a HY reference sample, calculated according to Eq. (1).

^b Relative amount of HY signal intensity (resonances at 165.6 and 163.3 ppm), obtained from lineshape analysis of ¹³C NMR spectra.

^c Calculated according to Eq. (2).

share of HY remained unreacted in both pastes and suspensions. The phase content of the phase to which the carboxylic resonance B was allocated could not be determined, since no reference sample was available.

3.1.6. Mass balance calculations

Mass balance calculations were done for paste and suspension samples cured for 12 months. The calculations yielded the HY content and the chemical composition of the residue, i.e. MgO, CO₂, and H₂O content bound in hydration products such as brucite and any other Mg-compound (if present). Tables 8 and S4 in the ESM summarize the results for pastes and suspensions, respectively. The amount of HY calculated by TGA for the 90/10 samples cured at 20 °C and for the 70/30 samples cured at 20 and 60 °C was crosschecked with results obtained from ¹³C CP-MAS NMR measurements (Table 7). The HY content between both techniques varied between 1 and 4 mass%. Since both analytical techniques used different routes to obtain the HY content, we judge the deviations to be within the expected error tolerances (a few mass%), thus, verifying the other techniques approach.

The lowest HY content was calculated by mass balance calculations for 90/10 samples, while samples with a high initial HY content, e.g. 20/80 samples exhibited much higher HY content. Calculation of reaction degrees of HY on basis of TGA data showed that a lower HY content in the unhydrated sample resulted in a higher reaction degree of HY. For the paste samples, the highest reaction degree was calculated for the 90/10 sample (56.9 %), followed by 70/30 pastes with reaction degrees between 16.3 and 20.4 %, and 50/50 and 20/80 samples exhibiting even lower reaction degrees between 6.0 and 11.1 %.

Chemical compositions of residues (MgO, CO₂, and H₂O not bound in HY) given in mass% oxide content were converted in mole percentages to give estimations of the stoichiometry. The results of the chemical compositions of the residues obtained for each sample hydrated for 12 months were plotted into a ternary MgO-CO₂-H₂O diagram (Fig. 14). The chemical composition of the residues was dominated by MgO and H₂O, and in addition, was close to the chemical formula of brucite. Carbonate (expressed as CO₂ oxide content) in the residues was present only in small amounts: 1.4–2.8 wt% CO₂ for pastes and 2.0–5.4 wt% CO₂ for suspensions.

3.1.7. Liquid phase analyses of filtered suspensions

Fig. 15a–c shows Mg concentration, inorganic carbon concentration, and pH of 100/0, 90/10, 70/30, 50/50, and 20/80 suspensions cured at 20 °C. Corresponding data are listed in Table S5 in the ESM additionally including aqueous total concentrations of other elements (Na, K, Ca, S, Cl). Mg concentration (Fig. 15a) for the 100/0 samples was low; below 0.5 mM for all hydration times (1, 2, 4, 6, and 12 months). This can be explained by the relatively low solubility of brucite ($\log K_s = 17.05 \pm 0.2$ (25 °C) [59]). Since the 100/0 samples did not contain any HY, practically no inorganic carbon was detected (Fig. 15b). pH of the 100/0 sample measured after 1 and 2 months (Fig. 15c) was 10.6–10.7, which was close to the pH calculated with GEMS (pH = 10.6). However, the pH continuously dropped during the next months to 10 (measured after 12 months). Although sample vessels were practically full with no air left above the solutions and the vessels were sealed properly, carbonation due to CO₂ in the atmosphere could have led to a constant decrease of pH. Another possible carbonate source in the solutions were inorganic carbon rests from the manufacturing process of the precursor (lab-grade brucite) used to obtain MgO (see Table 1).

IC measurements of MgO/HY suspensions of different age yielded Mg concentrations between 1.0 mM (1 month) and 1.5 mM (12 months). Samples of higher age showed in general higher Mg concentrations than younger samples. Mg concentration was observed to be higher for samples with higher initial HY content, e.g. 20/80 suspensions, and lower for samples with low HY amount (90/10). Trends observed for Mg concentration were found to be valid for inorganic carbon content as

Table 8

Results of mass balance calculations of hydrated 90/10, 70/30, 50/50, 20/80 pastes cured for 12 months.

Binder composition	90/10	70/30					50/50	20/80			
Curing temperature	20 °C	7 °C	20 °C	40 °C	60 °C	20 °C	7 °C	20 °C	40 °C	60 °C	
Initial HY content [mass%]	10	30	30	30	30	50	80	80	80	80	
HY content calculated by TGA [mass%]	3.0	17.6	18.4	18.3	18.9	35.6	68.4	69.1	66.7	68.3	
HY content calculated by ¹³ C NMR [mass%]	1.8	n.d.	16.2	n.d.	16.5	n.d.	n.d.	n.d.	n.d.	n.d.	
Residual MgO [mass%]	63.8	53.5	52.8	54.3	54.7	42.0	20.9	20.2	21.8	21.3	
Residual CO ₂ [mass%]	1.5	1.7	1.4	1.6	1.4	1.7	2.1	1.6	2.8	2.4	
Residual H ₂ O [mass%]	31.7	27.2	27.5	25.8	25.0	20.7	8.7	9.1	8.8	8.0	
Mol norm MgO [–]	1	1	1	1	1	1	1	1	1	1	
Mol norm CO ₂ [–]	0.021	0.029	0.023	0.027	0.024	0.037	0.092	0.074	0.118	0.101	
Mol norm H ₂ O [–]	1.113	1.136	1.163	1.060	1.023	1.102	0.928	1.001	0.900	0.840	

well (Fig. 15b): Inorganic carbon content, which varied between 1.1 mM and 1.6 mM, was higher for samples of higher age and for samples with higher initial HY content. 90/10 suspensions showed particularly high deviation of inorganic carbon content between samples of different age, while all other MgO/HY suspensions showed very similar inorganic carbon concentration within samples of the same binder composition. Only one measurement of a 20/80 suspension cured for 4 months showed an anomalous concentration (likely an outlier) in comparison to the rest of the samples of different age.

Results of pH measurements of MgO/HY suspensions are presented in Fig. 15c. pH values were between 10.0 and 10.3 for MgO/HY suspensions, except two measurements of 6 months old 50/50 and 20/80 suspensions (values were slightly lower compared to the others, probably outliers). Since MgO/HY samples were initially mixed according to

different MgO to HY ratios, hence, having different chemical compositions, notable differences in pH could have been expected. However, dissolution of HY and release of carbonate into the solution must have led to the formation of a carbonate buffer system responsible for the similar pH of MgO/HY suspensions. The fractional amount of carbonate species (H_2CO_3 , HCO_3^- , and CO_3^{2-}) can be deduced from pH. Dissolution reaction of HCO_3^- to H^+ and CO_3^{2-} yields a pK_a value of 10.38 ($\text{pK}_a = -\lg([[\text{H}^+] + [\text{CO}_3^{2-}]]/[\text{HCO}_3^-])$) at 20 °C, $p = 1$ atm [60]. The pK_a value is close to the measured pH of the MgO/HY suspensions, indicating that the two dominant carbonate species in these samples were HCO_3^- and CO_3^{2-} , which stabilized the pH around the pK_a value and formed a buffer system.

Liquid phase data retrieved from 70/30 and 20/80 suspensions hydrated for 12 months at 7, 20, 40, and 60 °C is displayed in Fig. 16a–f

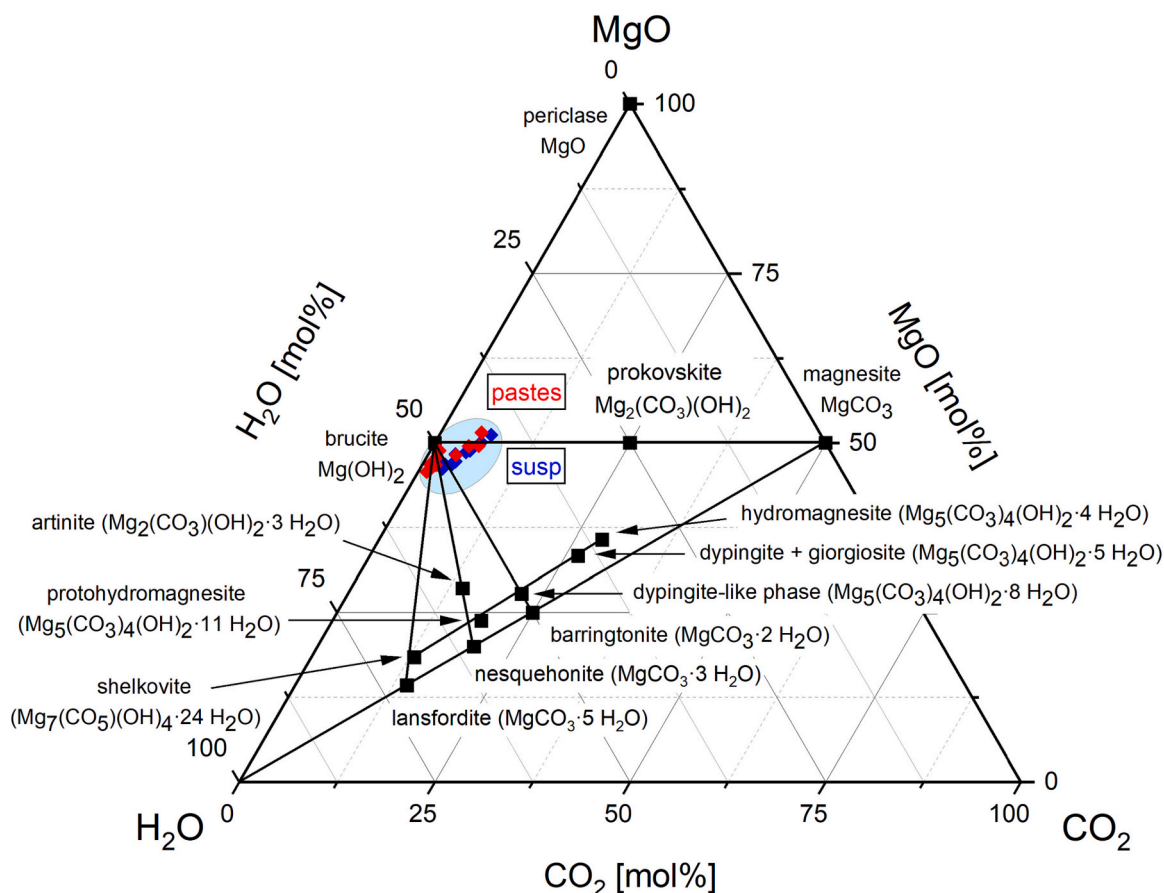


Fig. 14. Ternary MgO- CO_2 - H_2O diagram. The diagram shows HMCs with known chemical formulae (black) and bulk compositions of the solid residues (HY content has been subtracted) calculated by TGA of hydrated pastes (red) and suspensions (blue) cured for 12 months. Binder compositions and curing temperatures were not distinguished between the samples, since no systematic trend was found. (For interpretation of the references to color in this figure legend, the reader is referred to the web version of this article.)

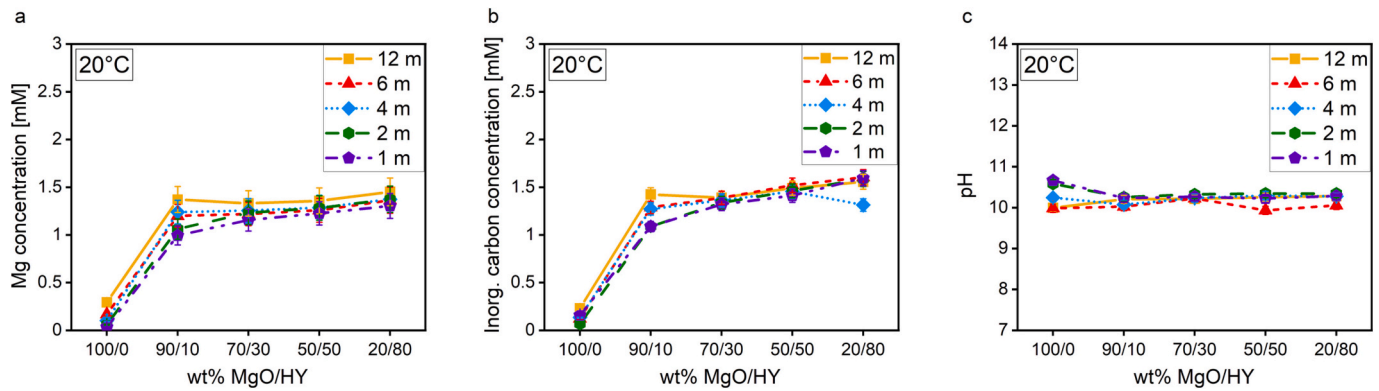


Fig. 15. (a) Mg concentration, (b) inorganic carbon concentration, and (c) pH of 100/0, 90/10, 70/30, 50/50, and 20/80 suspensions hydrated for 1, 2, 4, 6, and 12 months at 20 °C.

(omitting Na, K, Ca, S, Cl total concentrations). Data from the figure including the other elements measured by IC are listed in Table S6 in the ESM. Mg concentrations of 70/30 suspensions (Fig. 16a) increased steadily with time, the lowest Mg concentration was measured for samples cured for 1 month, the highest for samples cured for 12 months. Not only age, but also temperature had an effect on Mg concentration: Samples cured at 40 and 60 °C for 12 months reached higher Mg concentrations than samples cured at 20 °C. Especially samples cured at 60 °C showed a steep increase in Mg concentration already after 2 months of curing and reached the highest concentration measured for all samples of that series. A similar observation was made for the inorganic carbon concentration (Fig. 16b); where carbon concentration of samples cured at 7, 20, and 40 °C was lower than for samples cured at 60 °C after 6 and 12 months of hydration. The higher Mg and inorganic carbon concentrations at 60 °C can be explained by a higher solubility of the corresponding Mg-phases at higher temperature.

The effect of temperature was more pronounced for 70/30 suspensions than for 20/80 samples. Mg (Fig. 16d) and inorganic carbon concentrations (Fig. 16e) of 20/80 suspensions did not show a notable

increase of concentration at 60 °C. Results of pH measurements (expressed as OH^- concentration) of 70/30 and 20/80 suspensions are shown in Fig. 16c & f. OH^- concentrations were higher for samples cured at 7 °C and lower at 60 °C. pH of the 70/30 sample cured at 40 °C for 4 months was rather low, resulting in a low OH^- concentration (outlier in the diagram).

ESI of brucite and natural HMCs such as nesquehonite, lansfordite, artinite, HY, and dypingite were calculated with GEMS. ESI of suspensions cured at 7, 20, 40, and 60 °C were plotted in Fig. 17a–d, respectively. Magnesite was always strongly oversaturated (data not shown), but its precipitation is kinetically hindered at ambient conditions. ESI values indicated that artinite, brucite, and HY were oversaturated or close to saturation ($\text{ESI} \geq 0$). Calculation of ESI of nesquehonite, lansfordite, and dypingite yielded values indicating that those phases were undersaturated and not expected to form in MgO/HY suspensions ($\text{ESI} \leq -0.5$).

The formation of brucite, artinite, and the stabilization of HY in MgO/HY blends were predicted by thermodynamic modeling as detailed in Winnefeld et al. [16]. Calculation of the ESI for HY showed that the

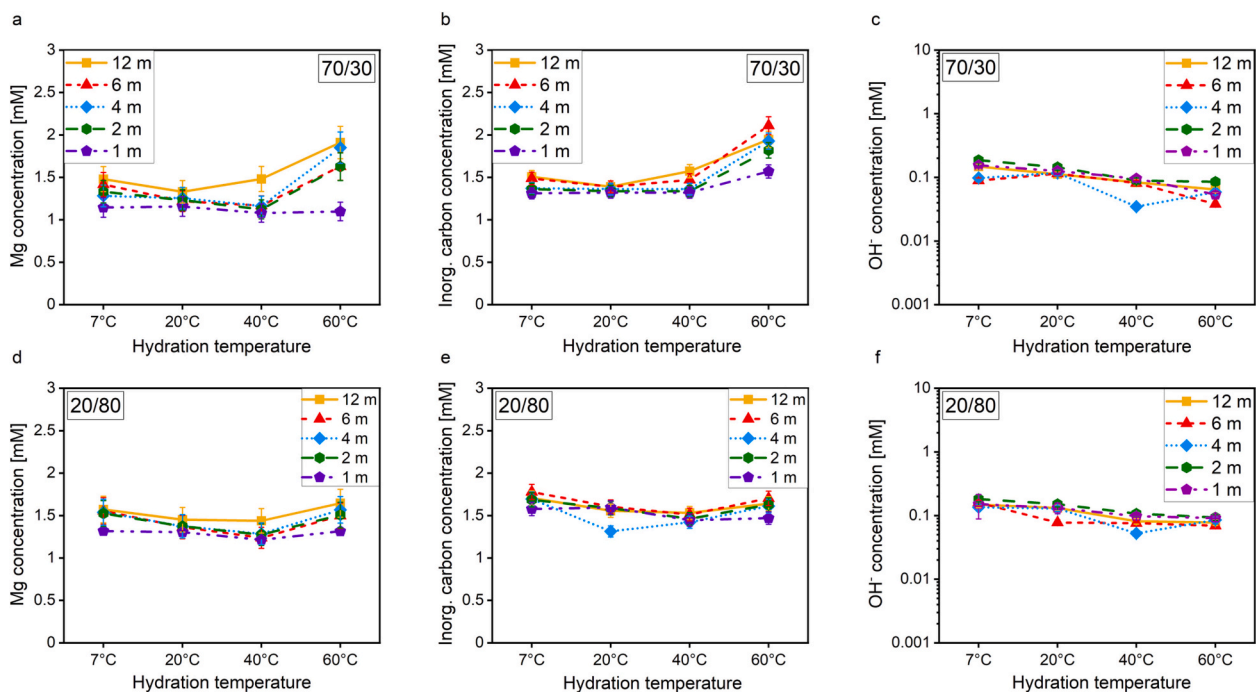


Fig. 16. (a) Mg concentration, (b) inorganic carbon concentration, and (c) OH^- concentration of 70/30 suspensions hydrated for 1, 2, 4, 6, and 12 months at 7, 20, 40, and 60 °C. (d–f) Data obtained for 20/80 suspensions.

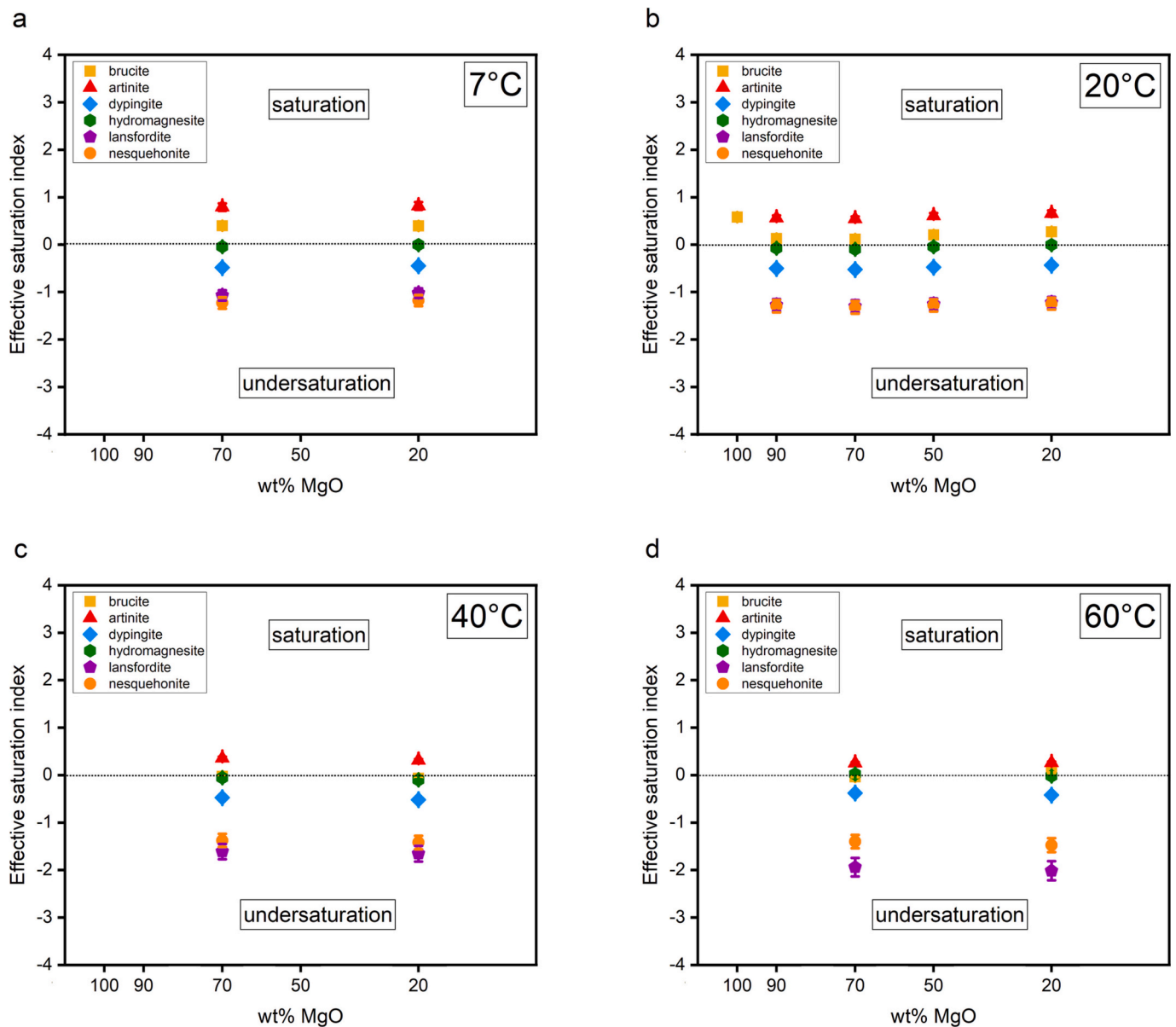


Fig. 17. Effective saturation indices (ESI) of common HMCs calculated for MgO/HY suspensions cured for 12 months at a) 7 °C, b) 20 °C, c) 40 °C, and d) 60 °C. Error was estimated to be 10 %.

phase was stable from a thermodynamic point of view, which matched with the experimental results. Artinite formation was neither observed in the study of Winnefeld et al. [16] nor in the present study, suggesting a kinetic hindrance of artinite formation.

4. Discussion

4.1. Solid phase assemblage

Isothermal calorimetry showed that HY significantly accelerated hydration of MgO/HY pastes at early age. The highest heat flow and cumulative heat was recorded for pastes with a high MgO content, identifying MgO as the main binder component driving forward hydration of MgO/HY blends. Most of MgO reacted already after one month of hydration and reaction was complete after four months, as evident from XRD data.

HY did not react completely, however, its partial dissolution implicated that carbonate ions were incorporated into a hydration phase. FTIR, Raman spectroscopy and ^{13}C CP-MAS NMR measurements verified

the presence of such an additional carbonate phase besides HY: FTIR of MgO/HY blends showed a weak band at 1712 cm^{-1} , which could not be allocated to any known HMC described in literature. In the Raman spectra, three bands of unknown origin were identified at 1028, 1048, and 1070 cm^{-1} . Since bands observed by FTIR and Raman spectroscopy in this study were at wavenumber ranges typical for HMCs, we postulate that these signals were related to a phase, which incorporated the carbonate released from the reacted HY. ^{13}C CP-MAS NMR delivered further evidence of an additional carbonate with a chemical shift at 173 ppm. Although ^{13}C CP-MAS NMR is a powerful tool to identify carbonates [55,56], the signals could not yet be attributed to any known HMCs.

The XRD patterns did as well not reveal the presence of HMCs. The only hydration product found in XRD was a poorly crystalline form of brucite, whose reflections were much broader in comparison to a crystalline brucite reference. Furthermore, XRD showed that the 001 reflection ($2\theta = 19.3^\circ$, $d = 4.60\text{ \AA}$) of this brucite was shifted towards higher 2θ angles in the samples cured at 7 and 20 °C compared to the pure crystalline brucite, indicating a smaller d-spacing of the

crystallographic (001) plane. Brucite's hydroxide sheets are arranged perpendicular to the crystallographic c-axis [61]. A smaller d-spacing of (001) planes results in a smaller interlayer distance. This alteration of the crystal structure of brucite can for example be explained by a change of its chemical composition having an impact on its layered structure. Deviations in d-spacing observed in layered structures are well known for clay minerals, where layer displacements (stacking faults) and/or layer rotation (turbostratic disorder) create complex diffraction patterns [62,63]. Although not described in literature yet, it is possible that brucite is affected in a similar way as clay minerals due to the incorporation of water and carbonate.

In addition to the low crystalline brucite, a hump between $2\theta = 16.1\text{--}16.8^\circ$ ($d = 5.27\text{--}5.50 \text{ \AA}$) of unknown origin was detected by XRD in accordance to literature [16,17]. The 2θ position of the hump was close to the 001 reflection of the low crystalline brucite. In samples cured at 7 and 20°C , the 2θ positions of the hump and of the 001 brucite reflection slightly differed ($\Delta(2\theta) = 2.5\text{--}3.2^\circ$). However, at 40°C the maxima of the hump and of the 001 brucite reflections shifted closer together and also closer to the position of the 001 reflection of the crystalline brucite reference, decreasing the distance in the diffraction pattern between both to $\Delta(2\theta) = 1.8\text{--}1.9^\circ$. At 60°C , the hump was not present anymore, while the 001 brucite reflection of the hydrated sample is at the same 2θ position than for the crystalline brucite reference. It seems that the hump and the 001 reflection of the low crystalline brucite merged into one single reflection at 60°C at the same 2θ position as for the crystalline brucite reference. Thus, it can be suggested that both the hump and the 001 brucite reflection are related to the same phase.

As FTIR, Raman and ^{13}C CP-MAS NMR spectroscopy clearly showed that an additional carbonate phase must be present, however, no HMC was found, it follows that the poorly crystalline brucite must contain carbonate. TGA/FTIR data of 90/10 pastes supports this theory: A strong CO_2 signal was measured by FTIR in the exhaust gases during the TGA measurement in the temperature range, where crystalline brucite typically decomposes ($300\text{--}480^\circ\text{C}$). Since the main HY decarbonation peak occurred at higher temperatures ($500\text{--}550^\circ\text{C}$) and in addition, its CO_2 signal was lower in intensity than the CO_2 signal during decomposition of brucite, unreacted HY could be excluded as potential source for this CO_2 signal. Hence, the CO_2 , which was released in the temperature range between 300 and 480°C , originated from the poorly crystalline brucite. A carbonate-containing brucite would on the one hand explain the additional, so far in literature undescribed carbonate signals in FTIR,

Table 9

Estimated thermodynamic properties at 25°C of the hypothetical phase: $[\text{MgCO}_3]_{1/36}[\text{Mg}(\text{OH})_2]_{35/36}[\text{H}_2\text{O}]_{1/36}$ representing a possible composition of HCB.

Thermodynamic properties	Values
$\log K_S^{\circ a}$	-11.08
V_m^b	$25.22 \text{ cm}^3/\text{mol}$
$\Delta_f G^\circ$	-844.31 kJ/mol
$\Delta_f H^\circ$	-936.8 kJ/mol
$S^\circ b$	$64 \text{ J/(mol}\cdot\text{K)}$
$C_p^{\circ b}$	$78 \text{ J/(mol}\cdot\text{K)}$

^a $K_S^\circ ([\text{MgCO}_3]_{1/36}[\text{Mg}(\text{OH})_2]_{35/36}[\text{H}_2\text{O}]_{1/36}) = \{\text{Mg}^{2+}\} \cdot \{\text{OH}^-\}^{70/36} \cdot \{\text{CO}_3^{2-}\}^{1/36} \cdot \{\text{H}_2\text{O}^0\}^{1/36}$, $\{\}$ denotes the activity of the respective species.

^b Molar volume, entropy and heat capacity were estimated based on [35] from brucite and HY.

Raman spectroscopy and ^{13}C CP-MAS NMR, and on the other hand explain the strong CO_2 signal in the TGA decomposition range of the brucite.

Besides the CO_2 release between 300 and 480°C , a notable water loss was measured by TGA between 30 and 160°C , which was observed by Winnefeld et al. [16] as well. As carbonate-containing brucite is probably the only hydration product present, it can be concluded that this water was bound as a loosely bound kind of "gel water" by the carbonate-containing brucite. Thus, we suggest that a *hydrous carbonate*-containing brucite (HCB) is the major hydrate, which forms in hydrated MgO/HY blends.

4.2. Suggested composition and thermodynamic data of HCB

Calculation of ESI from liquid phase analysis data showed that only brucite, artinite and HY were stable from a thermodynamic point of view. However, artinite was not experimentally observed. Liquid phase analysis data was further used to retrieve thermodynamic data of HCB. For this, a hypothetical chemical composition was chosen to represent HCB according to the calculated chemical compositions of the residues from pastes and suspensions obtained from TGA experiments. Following the restrictions given by results from mass balance calculations, the chemical formula of the hypothetical phase was narrowed to the following equation: $x \text{ MgCO}_3 \cdot y \text{ Mg}(\text{OH})_2 \cdot \text{H}_2\text{O}$ ($x = 0.5\text{--}1$, $y = 3.5\text{--}35$). Due to multiple possible formula stoichiometry, the hypothetical phase

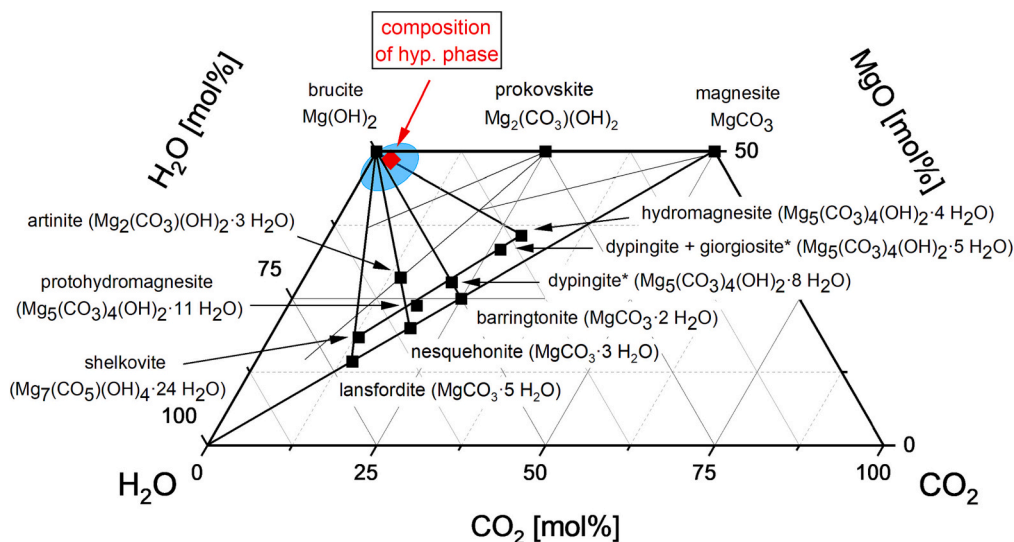


Fig. 18. Quaternary $\text{Mg}(\text{OH})_2\text{--MgCO}_3\text{--CO}_2\text{--H}_2\text{O}$ diagram. The hypothetical $\text{MgCO}_3\cdot 35\text{Mg}(\text{OH})_2\cdot \text{H}_2\text{O}$ phase, representing a possible composition of HCB, is marked by a red diamond symbol. The chemical composition of the hypothetical phase lies within the chemical compositions of residues obtained by TGA mass balance calculation (blue area).

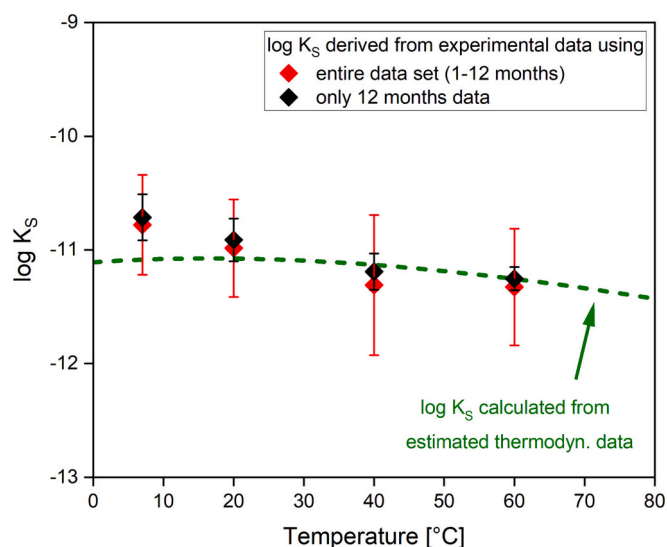


Fig. 19. Solubility products of the hypothetical phase $[\text{MgCO}_3]_{1/36} \cdot [\text{Mg}(\text{OH})_2]_{35/36} \cdot [\text{H}_2\text{O}]_{1/36}$; $K_s^\circ = \{\text{Mg}^{2+}\} \cdot \{\text{OH}^-\}^{70/36} \cdot \{\text{CO}_3^{2-}\}^{1/36} \cdot \{\text{H}_2\text{O}\}^{1/36}$ calculated from the thermodynamic data in Table 9 compared to the experimental IAP derived at 7, 20, 40 and 60 °C.

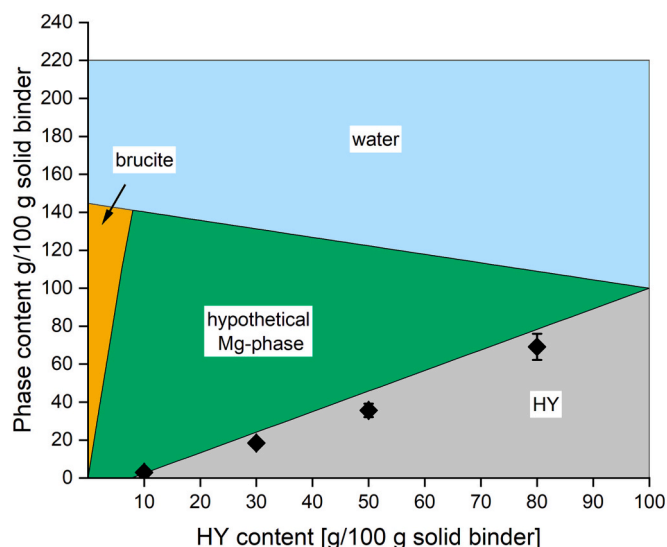


Fig. 20. Phase diagram showing the phase assemblage of stable Mg-phases in hydrated MgO/HY blends ($w/c = 1.20$) at 20 °C derived by thermodynamic modeling. Black diamonds mark unreacted HY content (TGA mass balance data) in MgO/HY pastes hydrated at 20 °C for 12 months, which is close to the calculated expected amount of unreacted HY from thermodynamic modeling. The hypothetical phase possibly represents chemical composition and thermodynamic properties of HCB.

$\text{MgCO}_3 \cdot 35\text{Mg}(\text{OH})_2 \cdot \text{H}_2\text{O}$ was selected as a model composition for HCB, reflecting an approximate chemical composition rather than an actual chemical compound with a well-defined chemical formula. Fig. 18 shows a quaternary $\text{Mg}(\text{OH})_2$ - MgCO_3 - CO_2 - H_2O phase diagram with known HMCs (colored in black) and the chosen hypothetical HCB composition (marked by a red diamond in the diagram).

The molar volume (V_m), entropy (S°), and heat capacity (c_p°) of the hypothetical phase were estimated according to [35] from brucite, HY and structural water. IAPs from the activity of Mg^{2+} , CO_3^{2-} , OH^- and H_2O^0 at 7, 20, 40 and 60 °C were calculated with GEMS using measured OH^- concentrations and total concentrations of Mg and inorganic carbonate. The IAPs determined at the different temperatures were used to

visually fit a solubility product at 25 °C, K_s^0 , and to calculate the corresponding Gibbs energy of formation ($\Delta_f G^\circ$) using GEMS. The apparent Gibbs free energy and the corresponding solubility products at other temperatures were derived based on the estimated entropy (S°) and heat capacity (c_p°) of the hypothetical phase according to Eq. (11). Table 9 lists all estimated or calculated thermodynamic properties of the hypothetical phase. The thermodynamic data was also used to model the changes in solubility product between 0 and 80 °C (Fig. 19) and compared to the IAPs calculated from experimental data at 7, 20, 40, and 60 °C after 1, 2, 4, 6, and 12 months (red diamonds) or using the data after 12 months only (black diamonds). Both data sets yielded values that lie on the solubility product curve within the error tolerances.

Finally, thermodynamic properties of the hypothetical phase were used to model the phase assemblage of hydrated MgO/HY pastes ($w/c = 1.20$) at 25 °C (Fig. 20). Brucite, the hypothetical phase, and HY were found to be thermodynamically stable. Other HMCs were not found to be stable when the hypothetical phase was included in the calculations. Formation of brucite was restricted from zero to 10 wt% HY (HY content of unhydrated binder), while HY was stable between 10 and 100 wt% HY. HY content determined from TGA experiments was plotted in Fig. 20, showing good agreement with the predicted unreacted HY content by modeling with GEMS. The hypothetical phase remained stable for all binder mix compositions, however, its highest phase content being calculated for 90/10 pastes, where brucite and HY were practically absent.

4.3. Implications of HCB formation in MgO/HY blends

Formation of HCB as the main hydration phase and its apparent stability in hydrated MgO/HY blends implies that a new cementitious Mg-phase has been found in this study. Previous works on the MgO/HY binder system [16,17] suggested the formation of an amorphous phase, which might be involved in strength development. Results of this study show that evidence for the formation of such an amorphous phase, i.e. amorphous hump observed in XRD, was mistaken for a reflection of HCB, which shows a splitting of its 001 reflection due to alteration of brucite's initial crystal structure. Formation of HCB in favor of brucite explains on one hand, which phase incorporated the carbonate from HY after dissolution, i.e. HCB, and on the other hand the change of crystal morphology leading to strength development. A separate amorphous Mg-phase was not found in this study and therefore disproves the theory that such a phase could be related to strength gain in the MgO/HY binder.

Mass balance calculations have revealed a possible chemical formula of HCB: $\text{MgCO}_3 \cdot 35\text{Mg}(\text{OH})_2 \cdot \text{H}_2\text{O}$, whose thermodynamic stability in MgO/HY blends was tested and found to be plausible. Due to a layered structure of HCB it is possible that the amount of incorporated water and carbonate might vary, thus, allowing different chemical compositions resulting in water and carbonate rich or poor HCB phases.

5. Conclusion

It was found that hydromagnesite (HY) partially dissolved during hydration of MgO/HY blends, leading to the release of carbonate. FTIR, Raman spectroscopy, and solid state ^{13}C CP-MAS NMR could not confirm the formation of a hydrated magnesium carbonate (HMC), which could have had incorporated the released carbonate. Instead, signals of an unknown carbonate-bearing phase were detected. However, only brucite was found as hydration product by XRD and TGA/FTIR.

TGA/FTIR experiments showed that CO_2 was released during the decomposition of brucite. Hence, it is evidenced that the carbonate released by HY was taken up by brucite. Furthermore, mass loss due to water release was detected at low temperatures, indicating that a kind of "gel water" was additionally bound by brucite. Thus, the uptake of water

and carbonate resulted in the formation of a *hydrous carbonate*-containing *brucite* (HCB) responsible for the carbonate signals measured with FTIR, Raman spectroscopy, and solid state ^{13}C CP-MAS NMR. The uptake of water and carbonate was associated with a loss of crystallinity, which was evident from a notable broadening of reflections in diffraction patterns. In addition, HCB's crystal structure exhibited a unit cell contraction parallel to the crystallographic c-axis, resulting in a smaller interlayer spacing than in conventional crystalline brucite as detected by a shift of the 001 reflection towards higher 2θ values. The alteration of brucite's initial crystal structure also resulted in the appearance of an additional hump in the XRD pattern, which is probably related to the stacking sequence of the hydroxide sheets in the brucite structure.

Liquid phase data obtained from MgO/HY suspensions by ion chromatography, pH and inorganic carbon measurements were used to calculate effective saturation indices of known HMCs. HY, which only partially reacted during hydration, was thermodynamically stable. Formation of artinite was predicted, but not observed by experiments, probably due to kinetic constraints. Other HMCs such as nesquehonite, lansfordite, and dypingite were undersaturated and were not found in the experiments.

A hypothetical phase with the formula $\text{MgCO}_3 \cdot 35\text{Mg}(\text{OH})_2 \cdot \text{H}_2\text{O}$ was proposed on basis of TGA mass balance calculations to represent the HCB for thermodynamic modeling. Thermodynamic properties of the hypothetical phase were estimated based on results obtained from liquid phase analyses. Thermodynamic modeling of the hydrate assemblage present in MgO/HY blends verified the stability of the hypothetical phase, thus, further supporting the formation of HCB.

Since HCB was identified as the main hydration phase in MgO/HY blends, its further characterization is necessary for understanding strength-building processes in such construction materials. Future research should focus on synthesis of HCB to validate brucite's capability for carbonate and water uptake. A pure phase could be used to retrieve crystallographic information or thermodynamic properties by dissolution experiments. In general, a systematic study to obtain HCB would enrich fundamental research done on the ternary MgO- CO_2 - H_2O chemical system.

CRediT authorship contribution statement

Alexander German: Conceptualization, Methodology, Validation, Formal analysis, Investigation, Data curation, Writing – original draft, Visualization. **Frank Winnefeld:** Conceptualization, Methodology, Writing – review & editing, Supervision, Funding acquisition. **Pietro Lura:** Writing – review & editing, Supervision, Funding acquisition. **Daniel Rentsch:** Investigation, Data curation, Methodology, Writing – review & editing. **Barbara Lothenbach:** Data curation, Methodology, Writing – review & editing.

Declaration of competing interest

The authors declare that they have no known competing financial interests or personal relationships that could have appeared to influence the work reported in this paper.

Data availability

Data will be made available on request.

Acknowledgments

Yiru Yan and Luigi Brunetti are acknowledged for their assistance in performing ion chromatography measurements. Furthermore, we thank Ellina Bernard for fruitful discussions of analytical results, in particular for TGA and ^{13}C CP-MAS NMR. The financial support of B. Lothenbach by the Swiss National Science Foundation (SNSF project no. TMAG-2_209222/1) and the grant for the NMR hardware (SNSF, grant no.

206021_150638/1) are gratefully acknowledged.

Appendix A. Supplementary data

Supplementary data to this article can be found online at <https://doi.org/10.1016/j.cemconres.2023.107304>.

References

- [1] A. Pisch, E.M. Gartner, M. Gimenez, V. Meyer, A novel atmospheric pressure approach to the mineral capture of CO_2 from industrial point sources, in: 13th Annual Conference on Carbon Capture, Utilization and Storage, Pittsburgh, Pennsylvania, USA, 2014.
- [2] W.J.J. Huijgen, R.N.J. Comans, Carbon Dioxide Sequestration by Mineral Carbonation, Literature Review Update 2003–2004 (Report), Energy Research Centre of the Netherlands, Petten, The Netherlands, 2005.
- [3] J. Sipilä, S. Teir, R. Zevenhoven, Carbon Dioxide Sequestration by Mineral Carbonation: Literature Update 2005–2007 (Report), Åbo Akademi University, Turku, Finland, 2008.
- [4] R. Zevenhoven, J. Kohlmann, CO_2 sequestration by magnesium silicate mineral carbonation in Finland, in: Second Nordic Minisymposium on Carbon Dioxide Capture and Storage, Göteborg, Sweden, 2001.
- [5] H. Downes, Ultramafic rocks, in: D. Alderton, S.A. Elias (Eds.), Encyclopedia of Geology, Academic Press, Amsterdam, The Netherlands, 2021.
- [6] A. Scott, C. Oze, V. Shah, N. Yang, B. Shanks, C. Cheeseman, A. Marshall, M. Watson, Transformation of abundant magnesium silicate minerals for enhanced CO_2 sequestration, Commun. Earth Environ. 2 (2021) 25.
- [7] H. Dong, E.-H. Yang, C. Unluer, F. Jin, A. Al-Tabbaa, Investigation of the properties of MgO recovered from reject brine obtained from desalination plants, J. Clean. Prod. 196 (2018) 100–108.
- [8] I. Singh, R. Hay, K. Celik, Recovery and direct carbonation of brucite from desalination reject brine for use as a construction material, Cem. Concr. Res. 152 (2022), 106673.
- [9] F.P. Glasser, G. Jauffret, J. Morrison, J.L. Galvez-Martos, N. Patterson, M.S. E. Imbabi, Sequestering CO_2 by mineralization into useful nesquehonite-based products, Front. Energy Res. 4 (2016), 3.
- [10] J. Morrison, G. Jauffret, J.L. Galvez-Martos, F.P. Glasser, Magnesium-based cements for CO_2 capture and utilisation, Cem. Concr. Res. 85 (2016) 183–191.
- [11] S.A. Walling, J.L. Provis, Magnesia-based cements: a journey of 150 years, and cements for the future? Chem. Rev. 116 (2016) 4170–4204.
- [12] E.M. Gartner, T. Sui, Alternative cement clinkers, Cem. Concr. Res. 114 (2018) 27–39.
- [13] S. Sorel, Improved composition to be used as a cement and as a plastic material for molding various articles, United States Patent 53,092, United States, 1866.
- [14] M.A. Shand, A. Al-Tabbaa, J. Qian, L. Mo, F. Jin, Magnesia Cements: From Formulation to Application, Elsevier, Amsterdam (The Netherlands), Oxford (United Kingdom), Cambridge (United States), 2020.
- [15] N. Vlasopoulos, C.R. Cheeseman, Binder composition, PCT Patent Application PCT/GB2009/001610, International Publication Number WO 2009/156740 A1 (12/30/2009). Novacem Limited, 2009.
- [16] F. Winnefeld, E. Epifania, F. Montagnaro, E.M. Gartner, Further studies of the hydration of MgO-hydromagnesite blends, Cem. Concr. Res. 126 (2019), 105912.
- [17] C. Kuenzel, F. Zhang, V. Ferrandiz-Mas, C.R. Cheeseman, E.M. Gartner, The mechanism of hydration of MgO-hydromagnesite blends, Cem. Concr. Res. 103 (2018) 123–129.
- [18] F. Zhang, Magnesium Oxide Based Binders as Low-carbon Cements, Department of Civil and Environmental Engineering, Imperial College London, London, UK, 2012 (PhD thesis).
- [19] F. Winnefeld, A. Leemann, A. German, B. Lothenbach, CO_2 storage in cement and concrete by mineral carbonation, Curr. Opin. Green Sustain. Chem. 38 (2022), 100672.
- [20] K.L. Scrivener, V.M. John, E.M. Gartner, Eco-efficient Cements: Potential, Economically Viable Solutions for a Low- CO_2 Cement-based Materials Industry (Report), UNEP, 2016.
- [21] M. Achternbosch, C. Kupsch, E. Niek, G. Sardemann, Are New Magnesia-based Cements the Future? Part 2: Novacem - An Assessment of New Developments, Cement, Lime, Gypsum (ZKG), Karlsruhe Institute of Technology, Karlsruhe (Germany), 2012, pp. 64–72.
- [22] N. Vlasopoulos, J.P. Bernebeu, Integrated process for producing composites containing magnesium, PCT Patent Application PCT/IB20 13/001536, International Publication Number WO 2014/009802 A2, Calix Limited, 2014.
- [23] E. Nduagu, J. Bergerson, R. Zevenhoven, Life cycle assessment of CO_2 sequestration in magnesium silicate rock – a comparative study, Energ. Convers. Manage. 55 (2012) 116–126.
- [24] F. Goff, G. Guthrie, B. Lipin, M. Fite, S. Chipera, D. Counce, E. Kluk, H. Ziock, Evaluation of Ultramafic Deposits in the Eastern United States and Puerto Rico as Sources of Magnesium for Carbon Dioxide Sequestration (Report), Los Alamos National Lab. (LANL), 2000 (United States).
- [25] V. Prigobbe, M. Hanchen, M. Werner, R. Baciocchi, M. Mazzotti, Mineral carbonation process for CO_2 sequestration, Energy Procedia 1 (2009) 4885–4890.
- [26] A. German, F. Winnefeld, P. Lura, Hydration of MgO/hydromagnesite blends, in: ICCM2021 11th ACI/Rilem International Conference on Cementitious Materials and Alternative Binders for Sustainable Concrete vol. 349, 2021, pp. 15–22.

- [27] R. Snellings, J. Chwast, O. Cizer, N. De Belie, Y. Dhandapani, P. Durdzinski, J. Elsen, J. Haufe, D. Hooton, C. Patapy, M. Santhanam, K. Scrivener, D. Snoeck, L. Steger, S. Tongbo, A. Vollpracht, F. Winnefeld, B. Lothenbach, RILEM TC-238 SCM recommendation on hydration stoppage by solvent exchange for the study of hydrate assemblages, *Mater. Struct.* 51 (2018) 172.
- [28] J.J. Thomas, S. Musso, I. Prestini, Kinetics and activation energy of magnesium oxide hydration, *J. Am. Ceram. Soc.* 97 (2014) 275–282.
- [29] D. Massiot, F. Fayon, M. Capron, I. King, S. Le Calvé, B. Alonso, J.O. Durand, B. Bujoli, Z. Gan, G. Hoatson, Modelling one- and two-dimensional solid-state NMR spectra, *Magn. Reson. Chem.* 40 (2002) 70–76.
- [30] E. Bernard, B. Lothenbach, C. Chlique, M. Wyrzykowski, A. Dauzeres, I. Pochard, C. Cau-Dit-Coumes, Characterization of magnesium silicate hydrate (M-S-H), *Cem. Concr. Res.* 116 (2019) 309–330.
- [31] B. Lothenbach, Thermodynamic equilibrium calculations in cementitious systems, *Mater. Struct.* 43 (2010) 1413–1433.
- [32] D.A. Kulik, T. Wagner, S.V. Dmytrieva, G. Kosakowski, F.F. Hingerl, K. V. Chudnenko, U.R. Berner, GEM-Selektor geochemical modeling package: revised algorithm and GEMS3K numerical kernel for coupled simulation codes, *Comput. Geosci.* 17 (2013) 1–24.
- [33] T. Wagner, D.A. Kulik, F.F. Hingerl, S.V. Dmytrieva, Gem-Selektor geochemical modeling package: TSolMod Library and data interface for multicomponent phase models, *Can. Mineral.* 50 (2012) 1173–1195.
- [34] Q. Gautier, P. Benezeth, V. Mavromatis, J. Schott, Hydromagnesite solubility product and growth kinetics in aqueous solution from 25 to 75°C, *Geochim. Cosmochim. Acta* 138 (2014) 1–20.
- [35] H.C. Helgeson, J.M. Delany, H.W. Nesbitt, D.K. Bird, Summary and critique of the thermodynamic properties of rock-forming minerals, *Am. J. Sci.* 278 (1978) 1–229.
- [36] J.W. Johnson, E.H. Oelkers, H.C. Helgeson, Supcrt92 - a software package for calculating the standard molal thermodynamic properties of minerals, gases, aqueous species, and reactions from 1 bar to 5000 bar and 0°C to 1000°C, *Comput. Geosci. UK* 18 (1992) 899–947.
- [37] W. Hummel, U. Berner, E. Curti, F.J. Pearson, T. Thoenen, Nagra/PSI chemical thermodynamic data base 01/01, *Radiochim. Acta* 90 (2002) 805–813.
- [38] E. Konigsberger, L.C. Konigsberger, H. Gamsjager, Low-temperature thermodynamic model for the system $\text{Na}_2\text{CO}_3\text{-MgCO}_3\text{-CaCO}_3\text{-H}_2\text{O}$, *Geochim. Cosmochim. Acta* 63 (1999) 3105–3119.
- [39] R.J. Hill, J.H. Canterford, F.J. Moyle, New data for lansfordite, *Mineral. Mag.* 46 (1982) 453–457.
- [40] R.A. Robie, B.S. Hemingway, Heat-capacities at low-temperatures and entropies at 298.15 K of nesquehonite, $\text{MgCO}_3 \cdot 3\text{H}_2\text{O}$, and hydromagnesite, *Am. Mineral.* 57 (1972) 1768–1781.
- [41] A.L. Harrison, V. Mavromatis, E.H. Oelkers, P. Benezeth, Solubility of the hydrated Mg-carbonates nesquehonite and dypingite from 5 to 35°C: implications for CO_2 storage and the relative stability of Mg-carbonates, *Chem. Geol.* 504 (2019) 123–135.
- [42] G. Raade, Dypingite, a new hydrous basic carbonate of magnesium, from Norway, *Am. Mineral.* 55 (1970) 1457–1465.
- [43] B.J. Merkel, B. Planer-Friederich, Groundwater Geochemistry. A Practical Guide to Modeling of Natural and Contaminated Aquatic Systems, Springer, Berlin, 2008.
- [44] C.G. Maier, K.K. Kelley, An equation for the representation of high-temperature heat content data, *J. Am. Chem. Soc.* 54 (1932) 3243–3246.
- [45] T. Oey, A. Kumar, J.W. Bullard, N. Neithalath, G. Sant, The filler effect: the influence of filler content and surface area on cementitious reaction rates, *J. Am. Ceram. Soc.* 96 (2013) 1978–1990.
- [46] L.A. Hollingbery, T.R. Hull, The thermal decomposition of natural mixtures of huntite and hydromagnesite, *Thermochim. Acta* 528 (2012) 45–52.
- [47] R.L. Frost, J.T. Klopogge, Infrared emission spectroscopic study of brucite, *Spectrochim. Acta A* 55 (1999) 2195–2205.
- [48] R.L. Frost, Raman spectroscopic study of the magnesium carbonate mineral hydromagnesite ($\text{Mg}_5(\text{CO}_3)_4(\text{OH})_2 \cdot 4\text{H}_2\text{O}$), *J. Raman Spectrosc.* 42 (2011) 1690–1694.
- [49] N.V. Chukanov, Infrared Spectra of Mineral Species, Springer, Dordrecht, Heidelberg, New York, London, 2014.
- [50] G.C. Jones, B. Jackson, Infrared Transmission Spectra of Carbonate Minerals, Chapman & Hall, London, New York, 1993.
- [51] H.C. Han, S. Hu, J.Q. Feng, H.L. Gao, Effect of stearic acid, zinc stearate coating on the properties of synthetic hydromagnesite, *Appl. Surf. Sci.* 257 (2011) 2677–2682.
- [52] P. Dawson, C.D. Hadfield, G.R. Wilkinson, The polarized infra-red and Raman spectra of $\text{Mg}(\text{OH})_2$ and $\text{Ca}(\text{OH})_2$, *J. Phys. Chem. Solids* 34 (1973) 1217–1225.
- [53] T.S. Duffy, C. Meade, Y.W. Fei, H.K. Mao, R.J. Hemley, High-pressure phase-transition in brucite, $\text{Mg}(\text{OH})_2$, *Am. Mineral.* 80 (1995) 222–230.
- [54] H.G.M. Edwards, S.E.J. Villar, J. Jehlicka, T. Munshi, FT-Raman spectroscopic study of calcium-rich and magnesium-rich carbonate minerals, *Spectrochim. Acta A* 61 (2005) 2273–2280.
- [55] J.K. Moore, J.A. Surface, A. Brenner, L.S. Wang, P. Skemer, M.S. Conradi, S. E. Hayes, Quantitative identification of metastable magnesium carbonate minerals by solid-state ^{13}C NMR spectroscopy, *Environ. Sci. Technol.* 49 (2015) 657–664.
- [56] J.L. Cui, D.L. Olmsted, A.K. Mehta, M. Asta, S.E. Hayes, NMR crystallography: evaluation of hydrogen positions in hydromagnesite by ^{13}C $\{^1\text{H}\}$ REDOR solid-state NMR and density functional theory calculation of chemical shielding tensors, *Angew. Chem. Int. Edit.* 58 (2019) 4210–4216.
- [57] S. Ishihara, P. Sahoo, K. Deguchi, S. Ohki, M. Tansho, T. Shimizu, J. Labuta, J. P. Hill, K. Ariga, K. Watanabe, Y. Yamauchi, S. Suehara, N. Iyi, Dynamic breathing of CO_2 by hydrotalcite, *J. Am. Chem. Soc.* 135 (2013) 18040–18043.
- [58] E. Bernard, B. Lothenbach, D. Rentsch, A. German, F. Winnefeld, Effect of carbonates on the formation of magnesium silicate hydrates, *Mater. Struct.* 55 (2022) 183.
- [59] Y.L. Xiong, Thermodynamic properties of brucite determined by solubility studies and their significance to nuclear waste isolation, *Aquat. Geochem.* 14 (2008) 223–238.
- [60] W. Stumm, J.J. Morgan, Aquatic Chemistry - Chemical Equilibria and Rates in Natural Waters, 3 ed., John Wiley & Sons, Inc., New York, 1996.
- [61] F. Zigan, R. Rothbauer, Neutronenbeugungsmessungen am Brucit, *Neues Jahrb. für Mineral. Abhandlungen* (1967) 137–143.
- [62] A.A. Coelho, J.S.O. Evans, J.W. Lewis, Averaging the intensity of many-layered structures for accurate stacking-fault analysis using Rietveld refinement, *J. Appl. Crystallogr.* 49 (2016) 1740–1749.
- [63] K. Ufer, G. Ii, R. Kleeberg, H. Stanjek, R. Dohrmann, J. Bergmann, Description of X-ray powder pattern of turbostratically disordered layer structures with a Rietveld compatible approach, *Z. Kristallogr.* 219 (2004) 519–527.